Vapor Phase Strengthening of Nickel-Based Alloys for Actively-Cooled Thermostructural Panels

by

Sara Jane Pérez-Bergquist

A dissertation submitted in partial fulfillment
of the requirements for the degree of
Doctor of Philosophy
(Materials Science and Engineering)
in The University of Michigan
2010

Doctoral Committee:

Professor Tresa M. Pollock, Chair
Professor J. Wayne Jones
Professor Anthony M. Waas
Patrick L. Martin, Air Force Research Laboratory

To my husband, who has completed my world and made me excited about our future.

To my father, who encouraged my curiosity and interest in understanding the world around me.

To my mother whose love and support is unrivaled.

Acknowledgements

There are a large number of individuals who have made it possible for me to complete the work for this thesis. I would like to acknowledge the following people for their assistance and support.

First, I would like to thank my advisor, Professor Tresa M. Pollock, for her insight and guidance throughout this process. I cannot thank her enough for her assistance and motivation during this project. I am honored to have been a part of the challenging and enriching work environment of her research group. She has been an inspirational role model both as a scientist and as a person.

The past and present members of the Jones and Pollock research groups also deserve sincere gratitude. Special thanks go to Chris Torbet who was always able to point me in the right direction and to my office mate Wen Tu, your support, friendship and insightful conversations helped broaden my horizons and made my time in the lab much more enjoyable. I would also like to thank Jessica Terbush for always being there for a good talk and a smile.

Also the support for this work provided by the Department of Naval Research, grant number N00014-05-1-0439 is gratefully acknowledged.

Table of Contents

List of Tables

List of Figures

Abstract

Actively cooled thermostructural panels for use in emerging hypersonic flight systems require the use of advanced materials able to support substantial loads at elevated temperatures. A major challenge in this advancing technology is identifying formable structural materials that are strong, tough and oxidation resistant. For thermostructural panels to be optimized for low mass with an appropriate combination of mechanical strength and cooling capacity, the panel is required to have a thin-walled geometry. Advanced, high strength cast Ni-based alloys have attractive properties, but the fabrication of sub-millimeter walls with conventional casting processes would be extremely challenging. The purpose of this study is to develop a new processing path that would result in a rectangular channeled panel made of a nickel-based precipitation strengthened alloy in a previously unobtainable thin-walled geometry suitable for active cooling. Beginning with thin sheets of Ni-based solid-solution alloys and subsequently strengthening the material by vapor phase aluminization combined with an annealing treatment, this objective is accomplished. This study included selection of a wrought nickel-based alloy as the base substrate for panel fabrication, definition of a goal $\gamma + \gamma'$ microstructure, fabrication of rectangular channeled panels, and testing of the actively cooled panels at high temperature. Thermodynamic, material strength, diffusion, and panel thermomechanical stress models were integrated to determine an optimized geometry and microstructure for the strengthened panel. Panels were fabricated with the

optimized geometry and tested at high temperature with active cooling in both the as-fabricated and strengthened states. The strengthened panel was able to withstand a temperature 478 °C higher than the as-fabricated panel prior to failure indicating the increase in strengthening and temperature capability possible with this process.

Chapter 1

Introduction

1.1 Background

The National Aerospace Initiative (NAI) has provided milestones to bring to reality air-breathing hypersonic flight. This could be achieved using a scramjet (supersonic combustion ramjet) engine. Air-breathing vehicles designed for hypersonic flight have highly loaded wings, hot control surfaces and an airframe that is highly integrated with the propulsion system. The scramjet of a hypersonic vehicle is actively cooled by the fuel making high-temperature Ni-based alloys, similar to those used in turbines, candidate materials. Metallic structures could also include non-leading edge "acreage" panels.

Metallic structures are desired, where possible, due to their high resistance to damage and the availability of a spectrum of relatively low cost manufacturing approaches. In the case of the scramjet engine, a thermostructural panel could be used. The panels must endure extremely demanding high-temperature (near 1000 °C) and oxidizing conditions when operating at up to Mach 8 flight conditions [1-4].

In the development of any vehicle for flight, including hypersonic vehicles, weight is always a concern. Thermostructural panels are possible solutions, allowing for the use of high-temperature metals while keeping the weight of the structures reasonable. These sandwich panels may be in the form of prismatic cores, honeycombs, or Kagomé structures; examples of these geometries are shown in Figure 1.1. To address the structural and heat flux requirements, the geometry of thermostructural panels can be optimized for a combination of mechanical strength and cooling capacity [5-7]. Thus fabrication approaches for a wide range of panel geometries are needed.

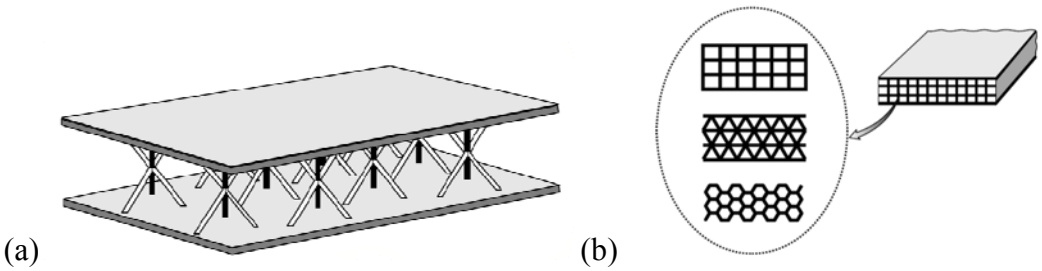

Figure 1.1: Examples of configurations for thermostructural panels. (a) Kagomé [8]. (b) Prismatic cores [2].

Nickel-based superalloys with high volume fractions of γ' (Ni_3Al) precipitates are often used in high-temperature aerospace applications and are conventionally cast into near net shape forms. The thin walls and geometrical complexity required of thermostructural panels to be used in a scramjet engine pose major challenges for conventional investment casting of nickel-based alloys [4]. While fabrication from thin gage sheet materials is an efficient alternative approach, most nickel-base alloys available in sheet form have

severely limited high temperature creep properties. Many refractory-lean γ-nickel alloys without precipitation hardening are readily processed into thin sheet and shaped at room temperature. Starting with thin wrought sheets of these alloys it is possible to fabricate panels with the required geometries; however, to be used as a thermostructural panel, the high-temperature mechanical properties of these alloys must be improved. Precipitation strengthening is the most efficient strengthening approach, but it must not interfere with the sheet processing operations.

In order to achieve a more optimal combination of high-temperature strength and complex geometrical structure, there must be a large volume fraction of γ′ precipitates in the material [9,10]. In order to achieve a higher volume fraction of γ′, it is necessary to increase the aluminum concentration. A processing method that consists of chemical vapor deposition of an aluminide layer with subsequent annealing to drive the aluminum through the sheet thickness has been developed. This process, referred to as vapor phase strengthening, results in precipitation strengthening of the alloy in a *post-fabricated* state. It is possible to produce the aluminide layer via pack cementation [11,12] and with the resulting concentration gradient of Al, subsequent annealing should result in a homogenization of the Al in the alloy [13].

This new processing method requires a suitable material to be used as the initial substrate. Ni-base alloys with good room temperature forming capabilities are likely candidates. This capability allows for the material to be fabricated in any of the geometries specified for optimization of the thermostructural panels. The extensive

research and development of nickel-based alloys for high-temperature application has yielded alloys with very advanced microstructures containing multiple populations of precipitates. It is important to choose an initial material that has major alloy constituents similar to advanced precipitation-strengthened materials, excluding the aluminum content, in order to have as much strengthening as possible. However, refractory alloying elements that result in high strengths may pose challenges to sheet processing [9,10]. Thus, tradeoffs in composition, strength and processing require further investigation.

1.2 Material Strengthening

Material strengthening occurs by inhibiting the motion of dislocations through the material. This can be achieved by multiple mechanisms, including solid solution strengthening, precipitation strengthening and/or grain size strengthening. In the case of solid solution strengthening, the material is strengthened without a change in the crystal structure of the alloy while precipitation strengthening involves the precipitation of a new phase in the alloy. Grain sizes are sensitive to the processing path with finer grains sizes beneficial for low temperature properties and coarser grain sizes beneficial for high temperature properties.

1.2.1 Solid solution and precipitation strengthening in Ni-base alloys

Solid solution strengthening is achieved by alloying the bulk with impurity atoms. These atoms will either substitute in the crystal structure or interstitially in solid solution. The

impurity atoms have a slightly different size than the base atoms and will impart local strains on the base alloy matrix. When a dislocation encounters this localized strain field, its motion is inhibited, requiring more force to keep it moving through the material [14]. Also, it is possible to reduce diffusion and provide strong lattice cohesion at high temperatures when the impurity atom additions are elements with high melting temperatures. Molybdenum and tungsten are typical alloying elements with Ni-based alloys [9,10]. This method can be very effective and can increase the strength dramatically.

Precipitation strengthening in Ni-based alloys typically involves the $L1_2$ phase γ'. Elements that stabilize this phase are primarily aluminum and titanium [9,10]. The precipitation of a new phase in the material will also inhibit dislocation motion. Instead of the dislocation only encountering a local strain field as with solid solution strengthening, the dislocation will also have to glide though a different crystal structure or else will be captured at the interface between the two phases. In Ni-based alloys, dislocations gliding through the FCC matrix (γ) shear the precipitates only at very high applied stresses. Upon encountering the $L1_2$ precipitate (γ') the dislocations may also be subject to thermally activated cross slip, which inhibits further glide [14].

In the γ phase, deformation occurs by dislocation glide on $a/2\langle 110\rangle\{111\}$ systems with the $a/2\left\langle 1\bar{1}0\right\rangle$ lattice vector as the shortest one available in the close-packed plane. In the $L1_2$ structure, the close-packed planes are again $\{111\}$, but the shortest lattice vectors, $a\langle 100\rangle$, do not reside in the $\{111\}$ plane. Therefore a single $a/2\langle 110\rangle\{111\}$ dislocation in

γ, although a perfect dislocation in that phase, cannot enter γ′ without a high energy anti-phase boundary fault being formed. This is because the vector required to restore the γ′ lattice to its perfect state is *twice* the Burgers vector of a single dislocation in γ. It follows that $a/2\langle 110\rangle\{111\}$ dislocations must travel in pairs through γ′. When there is a high volume fraction of γ′, multiple dislocations will be in the same γ′ precipitate. These dislocations are considered to be strongly coupled. With lower volume fractions or small γ′, there may only be one dislocation is in a precipitate at a time. In this case the dislocation pairs are weakly coupled [10].

Weak coupling refers to the case where the equilibrium spacing of the two paired dislocations is large in comparison with the particle diameter. The trailing dislocation is far enough behind the first that it will leave some faulted particles in its trail. While the first dislocation will remain at the precipitate-matrix interface until there is enough force to push the dislocation into the precipitate, since the second dislocation will restore order to the precipitates, it is energetically favorable for the second dislocation to enter the precipitate [10].

Strong coupling occurs when the γ′ particles are large and the spacing of the dislocation pairs becomes comparable to the particle diameter. Therefore, any given particle may contain a pair of dislocations. In this case the behavior is critically dependent upon the elastic repulsive force, which must be overcome if the trailing dislocation is to enter the γ′ particle. The optimum hardening in the nickel-based superalloys occurs for a γ′ particle size that lies at the transition from weak to strong coupling [10].

Due to the ordered character of the γ′, precipitation strengthening is much more effective than solid solution strengthening for Ni-based alloys. To increase the strength of the initial substrate alloy to be used in a scramjet engine, it is more effective to process the material in a way that results in precipitation the γ′ phase. This thesis proposes a new processing approach to achieve this.

1.2.2 Aging and strength optimization

Although the volume fraction of the precipitates is very important, optimization of properties requires control of precipitate size. The addition of aluminum (and to some extent tantalum and titanium) to a nickel-based alloy will increase the volume fraction of γ′ that is stable for a given temperature. Aging treatments will increase the size, but not the volume fraction of the precipitates. After the equilibrium volume fraction of precipitates is established during aging, decreasing the interfacial surface area can lower the total energy of this system. The lower total energy of the system is achieved through the growth of larger precipitates at the expense of smaller precipitates; this process is known as Ostwald ripening [15,16]. Because the precipitates will coarsen without changing the volume fraction, it is possible to tailor the microstructure and associated properties.

1.2.3 Strength modeling

Due to the extensive research on the microstructure of nickel-based superalloys, it is possible to predict the degree of strengthening that can be achieved with processing and microstructure control [9,10]. A model has been developed to account for contributions to strengthening due to solid solution, strong and weak pair coupling, as well as the Hall-Petch strengthening of the γ and γ' [17]. With this model it is possible to assess the volume fraction and morphology of γ' that could make a wrought nickel alloy a potential candidate for high temperature applications. The use of a model allows for a wide range of alloy compositions to be investigated without the time consuming process of physically processing individual alloys and mechanically testing many alloy variants.

With an appropriately strengthened alloy microstructure from the model, it is necessary to determine if that microstructure is feasible in a post-fabrication processing application. In order for there to be any γ' precipitation strengthening the aluminum concentration must be increased from the initial state of a solid-solution alloy. There are a variety of processes that can deposit aluminum on the surface of the alloy; the pack cementation process is the approach that will be employed in this research and this process will be discussed in the following section.

1.3 Pack Cementation

Pack cementation is a well-established chemical vapor deposition (CVD) technique that has been widely used for applying high-temperature protective diffusion coatings to superalloys used in the hot section of gas turbines [18-20]. The most developed pack cementation processes include aluminizing, chromizing, and siliconizing. Since the addition of aluminum to the alloys of interest will result in precipitation of γ', the aluminization process will be used.

The process consists of immersing the components to be coated in a powder mixture in a sealed or semisealed retort. The entire apparatus is placed inside a furnace and heated in a protective atmosphere to prevent oxidation. The exact time and temperature during the cycle are dependent on the required coating, coating thickness, and subsequent substrate heat treatment. The pack normally consists of the coating element source, in this case aluminum, an activator (typically a halide salt) and an inert filler material (most often alumina) to prevent the source from sintering at the processing temperature. At the treatment temperature the activator gives rise to a volatile aluminum subhalide (AlCl), which acts to transport solute material from the pack to the component to be coated, in this case depositing aluminum at the specimen surface by decomposition of the volatile aluminum compound [11, 18, 19].

For aluminization, the source can be either pure aluminum or an aluminum alloy, depending on the activity required in the pack. The implications of low and high activity packs will be discussed below. The process is simple to reproduce with a set of easily controlled parameters (temperature, time schedule and pack composition) ensuring a consistent process. The process is not 'line-of-sight' meaning the entire external surface of a component of complex shape can be uniformly coated including cavities and holes. Also, pack cementation is a relatively inexpensive process [20].

Although pack cementation is typically used to form a protective coating on the alloy, the process can be implemented for an alternative purpose. Both the high-activity inward diffusion of aluminum and the low-activity outward diffusion of nickel result in an increase in aluminum concentration on the surface of the coated alloy. It has been shown with a long heat treatment, it is possible to distribute the aluminum and nickel in a homogeneous manner [21-23]. This homogenization can allow for a new processing method of precipitation strengthened alloys.

1.3.1 Activator

Halide salts are typically used as the activator in pack cementation processes. Most often ammonium chloride (NH_4Cl) is used, yet there have been investigations into using alternative activators including aluminum fluorine (AlF_3), ammonium fluorine (NH_4F), sodium fluorine (NaF), sodium chloride (NaCl) and sodium iodine (NaI) [24, 25]. Although it is possible to use a variety of halide salts for the activator, it is only critical

that this salt can react with the aluminum in the pack to create an aluminum halide. This is critical as the high vapor pressure halide is the transport method for the aluminum from the pack to the substrate to be coated.

1.3.2 Pack Activity

The formation of aluminide coatings via pack cementation is carried out using either a high-activity or a low-activity pack. The activity is related to the concentration of aluminum in the Al-containing powder (Al source) used in the pack. If the aluminum source is greater than 60 atomic % aluminum, the corresponding pack is called a high-activity pack. Otherwise, the pack is referred to as a low-activity one. [11]

Typically a high-activity pack is a two-step process. This process consists of a relatively low temperature (~800 °C) aluminization step followed by a high temperature heat treatment to convert the microstructure to a state suitable for practical use as a protective coating [26]. A low-activity pack is typically aluminized at a higher temperature (~1100 °C) and does not require an additional heat treatment.

With a high-activity pack, there is predominantly inward diffusion of aluminum forming δ (Ni_2Al_3) and hyperstoichiometric (Al-rich) β (NiAl) in the substrate [20, 26, 27]. A low-activity pack, with predominantly outward diffusion of nickel, will form a hypostoichiometric β (NiAl) on the substrate surface. This indicates that aluminum is the

main diffusing element in δ and hyperstoichiometric β [28] while nickel is the main diffusing element in hypostoichiometric β [29].

High-activity packs, with the predominately inward diffusion, will maintain a consistent geometry and shape with the pre-coated substrate. In contrast, a low-activity pack, with the outward diffusion of Ni, will increase the thickness of the pre-coated substrate [27]. In the fabrication of thermostructural panels it is very important that the geometry of the panel be highly controlled, making the high-activity pack the preferred choice in this application.

1.3.3 Coating Microstructure

Due to the extensive use of the pack cementation process, there have been many studies on the microstructure of aluminide coatings on nickel alloys and their evolution with exposure to elevated temperatures for an extended period of time. For the high-activity pack, the δ (Ni_2Al_3) phase is present on the outer surface of the substrate [26]. This phase is quite brittle and decomposes at relatively low temperature, therefore, a coating made with a high-activity pack is typically subjected to further heat treatment prior to use [26, 27, 30].

The subsequent heat treatment that is typically used after a high-activity aluminization converts the brittle δ phase into the more oxidation resistant β phase. The diffusion process begins with continued inward diffusion of aluminum as the surface of the coating

still has similar activity to when the coating was being formed. Eventually the inward diffusion of aluminum will stop when it is no longer possible for β to form via aluminum diffusion. At this point, in order for continued formation of β, nickel migration must begin [26].

An extended heat treatment shows continued nickel diffusion from the substrate into the coating, reducing the aluminum content in the β phase [26]. Although this may be a concern when a stable β coating is desired, it shows that it is possible to use an aluminide coating followed by an extended high temperature heat treatment as a means to enrich a substrate with aluminum.

1.4 Sandwich Panels

The operating conditions of scramjet engines demand designs that include active cooling by the fuel and the use of lightweight materials that withstand extreme heat fluxes under oxidizing conditions. Metallic sandwich panels are optimally designed for minimum weight subject to prescribed combinations of bending and transverse shear loads and therefore are used to carry structural load as well as dissipate heat through solid conduction and forced convection [1]. The ability of sandwich panels to withstand substantial loads while simultaneously performing a thermal management function is highly desirable for flight systems due to their high efficiency from a weight standpoint.

Well designed structures using prismatic cores have additional potential due to their open structure for multi-functional applications. Unlike honeycomb core sandwiches or conventional stringer stiffened construction, prismatic core sandwich panels can serve as a heat transfer element while simultaneously carrying loads. Whenever possible, it is desirable to use metallic systems for their ability to deform plastically before failure. The materials selection list for high temperature applications is rather limited. Although some ceramics and intermetallics may have better mechanical properties at elevated temperatures, the low fracture toughness and complex fabrication methods can render them unacceptable. Nickel-based superalloys have proven to be very effective in turbine applications where high temperature performance and impact resistance are essential [9,10].

Although the panels considered here are of the prismatic core variety, there are still a number of variables that should be considered. The height of the panel, wall thicknesses and channel dimensions are among the geometrical design parameters. These design parameters will have optimum values that are dependent on the material of the panel. This would suggest that some strong materials that would not be considered in their bulk form due to weight could become candidate materials in a sandwich panel configuration.

Optimization models have been developed [3, 31] to properly compare potential materials for use in rectangular channeled prismatic core sandwich panels. These optimizations have shown that commercially available wrought nickel alloys will not compete with ceramic matrix composites for use in the sandwich panels due to the higher minimum

weight of commercially available nickel alloys [3, 31]. However, if the high temperature mechanical properties can be improved via post-fabrication processing, the nickel-based alloy could become competitive [32]. An increase in the maximum use temperature or improved strength at intermediate temperatures will decrease the overall weight of the panel for a specific flight condition [32]. It is also possible to improve the high temperature capabilities of a wrought nickel-based alloy by increasing the volume fraction of γ' precipitates [21-23].

1.5 Transient Liquid Phase Bonding and Brazing

As discussed in the previous section, an actively cooled thermostructural panel is desired for scramjet applications. Optimization techniques [5, 31-33] result in structures with wall thicknesses less than 500 μm, making casting a very challenging fabrication method. Possible alternative fabrication methods include assembling the structure from separate pieces, which requires a joining method such as TLP bonding or brazing.

Transient liquid phase joining, similar to brazing, is a joining process that produces high strength bond in heat resistant materials. The process uses a mating surface interlayer alloy, which temporarily melts and then resolidifies at the bond temperature to form a joint with characteristics resembling those of a solid-state diffusion bond. This method allows joints to be made in complex shaped parts with simple mating surface preparation [34].

As described above, the panel is fabricated before the processing of the material takes place. In order to fabricate the panel, the wrought sheet must be joined in the appropriate geometry. Brazing, which results in a solid-state diffusion bond, is a common way to repair turbine blades [34-36] and can be used to join the Ni-based substrate alloys. The braze material has a similar composition to the alloy that is to be joined with the addition of a fast diffusing melting temperature depressant, such as boron.

As the joint is heated, the braze alloy in the joint softens as it begins to approach its melting temperature, filling the gaps between the mating surfaces. The melting depressant has a very high diffusivity and quickly diffuses into the alloy substrate. As the melting point depressant diffuses away from the joint, the melting temperature of the filler metal increases, causing the melting temperature of the joint to increase. After a sufficient brazing time, the temperature depressant has reached a very low concentration due to diffusion and therefore the melting temperature of the joint increases to one similar to the substrate, thus forming a bond at a constant temperature. Typically the joint microstructure will resemble the base metal except for minor compositional and structural variations [34].

Although the bonds have good properties at this point, they may not be equivalent to that of the base alloy. If the part remains at the bonding temperature for longer times than needed for solidification, the bond can be homogenized both in composition and structure until it is essentially equivalent to the base metal [34]. For the current work, it should be noted that after the fabrication of the panels, the parts are exposed to long annealing

treatments where the limiting step is the diffusion of aluminum through the thickness of the panel walls. This would allow the homogenization step of the transient liquid phase bonding process to be incorporated into the interdiffusion step.

A growing application of brazing is the fabrication of multi-channeled metallic structures such as plate and plate/fin heat exchangers, fuel cells for power supply, catalytic converters and turbine seals. [37]. The applications above typically use amorphous brazing foil (ABF) or braze tape as the preferred filler metal.

In manufacturing superalloy turbine blades, the TLP bonding process is often used to attain complex shaped turbine blades with excellent cooling ability. The complex geometry allows for better cooling used to reduce fuel consumption with increased efficiency achieved by running at higher temperatures [38]. TLP bonding has also been shown to be applicable to turbine vane clusters and repairing compound turbine vanes [39].

The transient liquid phase process has been applied to a variety of systems simply by changing the filler alloy. Titanium, dissimilar metals, semiconductors and composites have all been successfully joined with this process [39] showing the wide range of uses possible. Transient liquid phase bonding is particularly attractive when fusion of the base metal must be avoided.

1.5.1 Temperature Depressants

In simple binary eutectic systems it is relatively easy to see the sharp decline in melting temperature as the concentration approaches the eutectic concentration and therefore the potential for brazing or TLP joining. For example, in the copper-silver system, the silver will act as a melting temperature depressant for copper [39]. If a layer of pure silver is sandwiched between a copper structure, upon heating to the bonding temperature, the silver interlayer and copper parent metal will undergo diffusion to form a liquid phase. As the dissolution progresses the composition moves up the liquidus lines from the eutectic. This will continue in the liquid until the concentration of the silver is diluted to the equilibrium concentration with the solid silver. At this point, solid-state diffusion dominates and the silver continues to diffuse into the copper [39].

This transient liquid phase process is not limited to binary eutectics, but can be applied to any system where the parent metal or alloy will form a relatively low melting temperature phase and has solubility for the melting temperature depressant [39]. It must melt at a temperature that the base metal can be exposed without experiencing deleterious effects, including melting. It is also important that the composition is such that the bond region solidify at the bonding temperature and become as chemically and microstructurally homogeneous as possible with the base metal [34]. The filler metals widely used in bonding processes of nickel alloys usually contain one or several melting point depressants such as silicon, boron, manganese, titanium and phosphorous to ensure proper liquid flow and wetting at the brazing temperature [34, 40].

1.5.2 Geometrical Control

Control of distortion is extremely important for successful brazing, especially in complex parts. For the current application, the precise control of geometry is critical. The geometry is specified for an optimized solution, which would be negated if the geometry were to distort in a significant way. The causes of distortion during furnace brazing have been investigated and control methods have been successfully used. Distortions can occur during fast heating, fast cooling and phase transformation (only important for ferritic materials) as well as due to stresses at temperature, residual stresses and dissimilar metals [41].

It is important to consider the possible causes of distortions so that they can be avoided during the brazing cycle. It is easy to eliminate the distortions due to rapid heating and cooling by simply choosing slower heating and cooling rates. In the current application, the fabrication of the panel takes place before any material processing; therefore specifics of the heating and cooling rate will not have an effect on the finished product. The possibility of distortions due to uneven heating will cause distortions resulting from residual stresses. Again, a slow heating and cooling rate will help eliminate these issues.

Distortion due to stresses at temperature relates to the ability of a part to support its own weight while at brazing temperature. This distortion is typically a result of low elevated temperature creep strength of the base material [41]. In this case, it is important to

consider the proper positioning of the part in the furnace to minimize the weight stresses. This can also be accomplished using fixtures. With the appropriate considerations, it is possible to fabricate a highly controlled geometry using a furnace brazing cycle.

1.6 Summary

A review of the literature has shown that there are a number of research areas that can be drawn upon and further developed to make the goals of this thesis feasible. A summary of the important research elements and their relevance is as follows:

- Strengthening of nickel-based alloys and processing paths to achieve strengthening are fairly well understood. In particular, the role of the $L1_2$ γ' precipitates has been widely studied. With the proper volume fraction and morphology of the precipitates, it is possible to substantially strengthen a wrought nickel-based superalloy for use in a high temperature regime. Although the proposed approach in this thesis begins with a wrought solid-solution nickel alloy, it is clear that significant strengthening can occur with increased aluminum and precipitation of the γ' phase. Without this strengthening, a solid-solution nickel alloy would not be feasible in the current application due to its relatively poor high-temperature properties.

- Through modeling, it will be possible to define high strength microstructures for a precipitation strengthened alloy with limited experimental process development

and/or mechanical testing of the alloy. This modeling allows for a more efficient means to develop new alloys and determine compositions and thermal processing paths. It is possible to determine the amount of aluminum that must be added to the solid-solution alloy in order for its use to be feasible in a high-temperature application.

- Pack cementation is a low-cost and highly repeatable process that will deposit aluminum on the surface of nickel alloys. Using a high-activity pack in the cementation process will yield a coating that is formed with the inward diffusion of aluminum into the component. It is possible to closely control the geometry of the part and microstructure of the coating by choosing an appropriate aluminum source. Extended heat treatment of nickel alloys with high-activity coatings has shown an increase in aluminum penetration and a decrease of the average aluminum concentration over the depth of aluminum penetration. This shows the aluminum in the coating will diffuse into the substrate altering the average composition of the alloy up to the penetration depth. This process has the potential to be used as a means to increase the average aluminum concentration of an alloy with a high concentration aluminum coating followed by a long annealing treatment without altering the geometry of the component.

- Transient liquid phase bonding and brazing are reliable joining methods that have been highly developed for high temperature applications. Many brazes and filler metals have been developed for nickel-based alloys. Structures have been

fabricated with very thin components. This would be applicable to the thin-walled prismatic core sandwich panel currently discussed, making the fabrication of such a panel feasible.

- Optimization tools for a rectangular channeled sandwich panel show how metallic structures can be competitive with ceramic or composite materials. Although the solid-solution nickel alloy is not very competitive from a weight standpoint for a fixed geometry, with the optimization model, there is room for improvement if the high temperature properties are improved. If the overall use temperature is increased or the strength at moderate temperatures is increased, the overall weight of the panel will decrease, making the metallic panel an attractive solution. With the model it is possible to determine the extent of strengthening and/or increase in use temperature that is necessary for a panel fabricated from a nickel-based alloy to be a feasible solution.

- By combining the information from the literature it is apparent that a new processing method can be developed to create a precipitation strengthened nickel based alloy in geometries that would be extremely challenging to cast. Without any of the technologies it would not be possible to create the final product. The joining technology allows for the fabrication of the panel, the coating technology allows for aluminum to be added to the alloy and diffused through. However, it would be unclear if this material is even a possible candidate for the panel without the modeling of its yield strength as well as the optimization of the panel with

these modeled properties. With the integration of these analytical and experimental approaches, initially designed for separate applications, it is possible to define new paths for processing and strengthening that are likely to be useful for high temperature thermostructural applications.

The following contributions are unique to this thesis work:

- Development of a new processing method to achieve a $\gamma + \gamma'$ precipitation strengthened nickel-based alloy in a previously unobtainable geometry.
- Integration of yield strength, panel geometry, and thermodynamic models to determine an optimized microstructure and geometry.
- Definition of the necessary combination of aluminization, homogenization and aging treatments to achieve the desired microstructure.
- Fabrication and high temperature testing of actively-cooled optimized panels determining benefits of the vapor phase strengthening process.

This thesis is organized as follows. Chapter 2 discusses the experimental materials and experimental procedures. Chapter 3 describes the feasibility of the new vapor phase strengthening method. Chapter 4 concerns the integration of models to determine a combination of microstructure and geometry needed to minimize the weight of a thermostructural panel. The vapor phase strengthening of alloy X-750 is discussed in

Chapter 5. Fabrication, strengthening, and high-temperature testing of thermostructural panels is described in Chapter 6. Finally, Chapter 7 summarizes with conclusions.

Chapter 2

Procedures

2.1 Experimental Materials

A variety of solid-solution nickel based alloys available in wrought sheet form have been investigated as potential starting materials for this process, including Haynes alloys X-750 and 214 as well as INCONEL alloys 625 and 693. All of these alloys are refractory lean with relatively large amounts of chromium. The major alloying components for each alloy are listed in Table 2.1.

Table 2.1: Major alloying components of nickel-based alloys (wt%) [42-45]

Alloy	Cr	Al	Fe	Ti	Nb	Co	Mo
H-X750	16	0.8	8	1	2.5	1	- -
H-214	16	4.5	3	- -	- -	- -	- -
IN-625	20 – 23	0.4	5	0.4	3 – 4	1	8 – 10
IN-693	27 – 31	2.5 – 4	2.5 – 6	0.5 – 2.5	- -	- -	- -

The thickness of the alloy sheets available varied from 200 μm to 2 mm in thickness. The only alloy available in the 200 μm thickness was INCONEL 625. While all other alloys used in this investigation varied thicknesses, they are all amenable to rolling as thin as 200 μm. Specimens of each alloy were cut with an electrical discharge machining (EDM) process to dimensions that were needed for each particular application, as reported below.

2.2 Aluminization

In order to properly carry out the aluminization process, an environmentally controlled furnace was created. A vertical tube furnace was used with a custom designed sealable quartz tube with moveable stage. Figure 2.1 is a photograph of the tube furnace. The 80 mm diameter tube extends over 250 mm above the furnace including a cool zone while maintaining the environmental control. The stage allows rapid movement between the hot and cool zones permitting the precise control of the aluminization time and/or aging treatments.

Figure 2.1: Photograph of custom made vertical tube furnace with a sealable quartz tube and movable stage.

As discussed above, an aluminide coating is deposited on the alloys to serve as an aluminum source for precipitation strengthening of the alloy. Samples were cut into rectangular pieces approximately 1 cm x 1.5 cm for initial aluminization experiments. Samples destined for tensile tests were cut into a dogbone shape consistent with sub-standard size specifications [46]. The gauge length was 2.5 cm long and 0.6 cm wide with a radius of curvature from the grip section of 5 cm. Although the aluminized sandwich panels were fabricated using two different methods, they were aluminized in a post-fabricated state consistent with procedures described below.

2.2.1 Pack Activity

A high activity pack was desired for all the aluminization procedures in this study. The primarily inward diffusion of aluminum in a high activity pack will minimally alter the geometry of the samples. The pack contained three components, an activator, aluminum source, and an inert filler. The activator was NH_4Cl (99.5% min), the aluminum source was aluminum powder (-40+325 mesh, 99.8%) and the inert filler was a-Al_2O_3 (99.9%). Consistent with the process described by Das et al. [27], the pack contained 3 wt% NH_4Cl, 15 wt% Al, and 82 wt% Al_2O_3. This pack content was consistent for all aluminization procedures in this study.

2.2.2 Aluminization Parameters

The rectangular samples were held in alumina trays with dimensions 2.5 x 2.5 x 1 cm completely surrounded by the pack powder mixture. The container was inserted into the cool zone in the vertical tube furnace equipped with argon flowing at 2 cm^3/s at a variety of temperatures and times. Once the furnace was at the specified temperature, the container was lowered into the hot zone of the furnace within 5 seconds and held for the specified time. At the end point, the container was lifted out of the hot zone and allowed to cool under flowing argon. Once the container was cooled, the samples were removed from the pack and ultrasonically cleaned to remove any pack powder from the surface of the sample.

Initial aluminization studies were carried out with the X-750 alloy over the temperature range of 800 °C to 1050 °C and times ranging from 5 minutes to 360 minutes (6 hours). These studies showed that the rate of aluminum deposition per square centimeter exhibited a logarithmic relationship with time for all temperatures tested. Experimental results for aluminizations performed at 850 °C had the best correlation with logarithmic trend-lines. For 850 °C the trend-line of the mass of aluminum added/cm^2 = 0.002ln(t)-0.0017. With these values it will be possible to calculate the aluminization time necessary to achieve an adequate aluminum source for the homogenization treatment.

2.3 Annealing and Aging

The samples and the panel were subsequently annealed in a vertical tube furnace with a flowing gas mixture of Ar + 3% H_2. Initially the samples were annealed to homogenize the Al concentration through the thickness of the thinnest samples. A homogenization cycle to achieve Al concentrations within 10 % of the average through the cross section was devised and will be discussed in more detail. Depending on the thickness of the samples, the homogenization times ranged from 150 hours to 200 hours at 1100 °C

Once the aluminum is distributed uniformly through the sheet cross section, aging treatments were performed to achieve the desired γ-γ′ microstructure. Two aging treatments were performed at 1075 °C for 17 minutes and at 980 °C for 2 minutes. The determination of these cycles will be discussed in more detail. These aging treatments were designed to create a microstructure with γ′ precipitates in two size distributions, 110

nm average diameter along with a second set of precipitates 25 nm in diameter. The samples were aged under flowing Ar in a vertical tube furnace that allowed for rapid cooling.

2.4 Microstructural Characterization

In order to characterize the microstructure at various steps of the process, a variety of techniques were employed, including scanning electron microscopy (SEM) and electronmicroprobe analysis (EMPA). Sample preparation and instrument operating conditions are given in the following sections.

2.4.1 Sample Preparation

Samples intended for the scanning electron microscope were mounted and using standard metallographic preparation techniques was ground and polished with a finishing step of 0.05 μm alumina. In order to obtain good contrast for the images of the microstructure, two etching solutions were utilized. An etching solution of 33% CH_3COOH, 33% H_2O, 33% HNO_3, and 1% HF was used to reveal the γ/γ′ microstructure, while an electrolytic etching solution of 11% H_3PO_4, 45.5% H_2SO_4 and 43.5% HNO_3 was used to dissolve the γ phase, leaving the γ′ phase intact. The electrolytic etch required a voltage of 7 volts and read approximately 0.2 amps/mm^2 during the etching process.

2.4.2 Scanning Electron Microscopy

Images of the microstructure for evaluation were taken using a Hitachi S-3200N SEM and a Phillips XL30 field emission gun SEM. Both of the SEMs were equipped with a removable back-scatter electron (BSE) detector.

2.4.3 Electron MicroProbe Analysis

Electron microprobe analysis (EMPA) using a CAMECA SX100 was performed to determine elemental concentration profiles across the sample thickness. Phases present were determined from wavelength spectrometry (WDS) combined with thermodynamic calculations from Pandat^{TM} which uses the CompuTherm database. Additionally, X-ray scans of post-aluminized material were conducted with an Enraf Nonius CAD4 Single Crystal X-Ray Diffractometer.

2.5 Mechanical Testing

To characterize the change in mechanical properties of the materials after the processing method described above, hardness data and tensile data were collected. Microhardness was chosen in order to quickly and accurately measure the gradient in properties through the cross section of thin samples. These data gave insights into the strengthening that took place for the initial alloys. Tensile tests were performed to characterize the change in yield strength for the optimized alloy microstructure.

Vickers microhardness was determined using a Buehler Micromet II digital Microhardness tester. Microhardness measurements were made on the surface of samples completely homogenized and through the sheet thickness for the thicker alloy samples at approximately 50 μm increments. Tensile samples were cut with an EDM process. The dimensions of the samples were 10 mm x 65 mm x 0.65 mm with a gauge section length of 25 mm. The radius of curvature from the grips down to the gauge section thickness was 5 mm. These samples were aluminized similar to the process described above.

The tensile samples were tested in tension with an Instron 5582 with a constant displacement of 0.05 mm/minute. The strain was measured with an Instron edge grip extensometer with a 12.7 mm gauge length. Measurements of Young's Modulus, Yield Strength and Ultimate Tensile Strength were preformed for all of the samples.

2.6 Oxidation Testing

Simple one-hour oxidation tests were performed on the initial samples in the as-received condition as well as post-homogenization. The cycle consisted of 1 hour at 1000 °C. The thickness of the oxidized layer was measured from SEM images.

2.7 Integrated Modeling

Thermodynamic alloy models, microstructure-based strength models and panel thermostructural stress analysis models were employed in an integrated manner to determine the desired microstructure and panel geometry. If the models were used separately, it is not guaranteed that a minimum weight structure would result. In order to find a structure optimized for minimum weight it is essential that microstructure and geometry are determined *together*. The models used included a thermodynamic model, a geometric model for a rectangular channeled sandwich panel, and a yield strength model all of which will be discussed in more detail in the following sections.

2.7.1 Thermodynamic Modeling

Thermodynamic modeling was performed for all the initial alloys and was also used to understand phase evolution through the various stages of processing. Pandat™ software, which uses the CompuTherm database, was utilized. Using the specific elemental variants for each alloy, pseudo ternary phase diagrams were calculated. The Pandat™ software was also used to determine the feasibility of potential precipitate distributions suggested by the strength model. This was determined by calculating the equilibrium volume fraction of the γ′precipitates over a range of temperatures.

2.7.2 Yield Strength Modeling

In order to determine which microstructure would be optimal for a minimum weight thermostructural panel, the yield strength of a range of potential microstructures was evaluated with a model developed by R. Kozar [17]. The model calculates the yield strength as a function of temperature based on the microstructure, chemistry and reference data. The strengthening mechanisms accounted for in the model are solid solution, grain boundary, weak pair coupling, and strong pair coupling. Input parameters include the composition of the matrix and the γ′ precipitates, grain size, total volume percent γ′ and up to three distinct populations of γ′ precipitates at different sizes.

The model was used once the alloy had been chosen for panel fabrication. The reference data used in the yield strength model was available from the manufacturer of the X-750 alloy. The model was run with either two or three populations of γ′ with sizes ranging from 10 nm to 600 nm for volume fractions ranging from 10 – 70%. The most promising data for each volume fraction was used in the panel geometry model.

2.7.3 Panel Geometry Modeling

A model developed by N. Vermaak et al. [32] optimizes the geometry of a rectangular channeled thermostructural panel for minimum weight given a required heat flux over the height of the panel. The geometrical variables for the panel in the model include wall thickness, face sheet thickness, and dimensions of the cooling channels. It is also

possible to consider a panel that takes into account the pressure in the combustor as well as the use of a thermal barrier coating. In this study the combustion pressure was taken into account, which corresponds to a panel that is not continuously supported, while the use of a thermal barrier coating was not used because the panels would be tested without a coating. The model will be discussed in more detail in Section 4.3.

These geometric optimizations are made based on the capabilities of a given material. To ensure that a global minimum mass was calculated, the material properties from a variety of microstructures were used as inputs for the model. Material inputs for the model included density, coefficient of thermal expansion, Young's modulus, conductivity, Poisson's ratio, maximum use temperature, reference yield strength (yield strength at 127 °C), and the yield strength change with temperature. All materials investigated in this study are nickel-based and have little variation in many material properties [40-43]. Therefore, for this study, the density, coefficient of thermal expansion, Young's modulus, conductivity and Poisson's ratio were held constant while the maximum use temperature, reference yield strength, and yield strength change with temperature were varied for each microstructure variant.

2.8 Panel Fabrication

Two approaches to panel fabrication were employed including brazing and electric discharge machining. Initially a panel was fabricated using a brazing method, as will be described below. It should be noted that this is not the only feasible way to fabricate a

thin-walled panel. Once an optimal geometry had been calculated it was determined that supplier availability were not adequate for the small scale of this study. Therefore an additional fabrication method was necessary to fabricate a panel with the optimized geometry. A combination of traditional machining and electrical discharge machining were used to create the optimized panel as described below.

2.8.1 Brazing

The alloy used to braze the panel pieces together was AMDRY DF6A, alloy composition in Table 2.2. This braze tape has a similar major alloying components to the Haynes alloy X-750. Some specimens were cut with an EDM into squares and rectangles for face sheets and panel webbing respectively. The face sheets were 52 mm x 52 mm with the webbing having dimensions 52 mm x 8.8 mm. The specimens used for the panel all had a thickness of 0.635 mm.

Table 2.2: Alloy composition of AMDRY DF6A in wt%. [47]

	Cr	Ta	B
AMDRY DF-6A	20	3	3.15

A 52 mm x 52 mm x 10mm panel with rectangular channels was fabricated with the pieces of X-750 sheet and AMDRY DF-6A braze tape. The braze tape was applied to the long edges of the panel webbing and subsequently attached to the face sheets. The pieces were held in place for the brazing cycle with a reusable fixture for high repeatability. The brazing cycle was performed with flowing Ar + 3% H_2 gas in a vertical tube furnace

consisting of a 20 minute hold at 450 °C, to remove the organics from the braze tape followed by a 30 minute treatment at 1200 °C to join the pieces.

2.8.2 Electric Discharge Machining

Once the optimized geometry had been determined from the integrated modeling, the thickness of the webbing and face sheets needed to be thinner than the material immediately available from commercial suppliers. In order to achieve the very thin walls for the optimized panel, it was necessary to EDM the channels of the panels. Four panels were created by starting with plate stock and traditionally machined to size with a 3-axis mill of 5.8 mm x 45 mm x 63.5 mm. The channels were created by drilling holes for the channels and cutting out the material with a wire EDM to create 5 channels with dimensions of 5 mm x 8.5 mm.

2.9 High-Temperature Panel Testing

In order to accurately determine the performance of the panels in conditions similar to those described in the optimization model, it is necessary to test the panel in a high-temperature environment. The temperature, pressure and flow rate parameters in the model can be replicated and varied. This allows for testing in more benign as well as more aggressive conditions.

2.9.1 Setup

Two of the panels were EDMed, aluminized, homogenized, and heat treated similar to the tensile samples described above. The remaining panels were kept in their as-fabricated state for comparison. The testing apparatus (see Figure 2.2) for the panels was designed to allow the panels to be heated on one side with an oxy-acetylene torch while being actively cooled by water flowing through the channels at a variety of pressures.

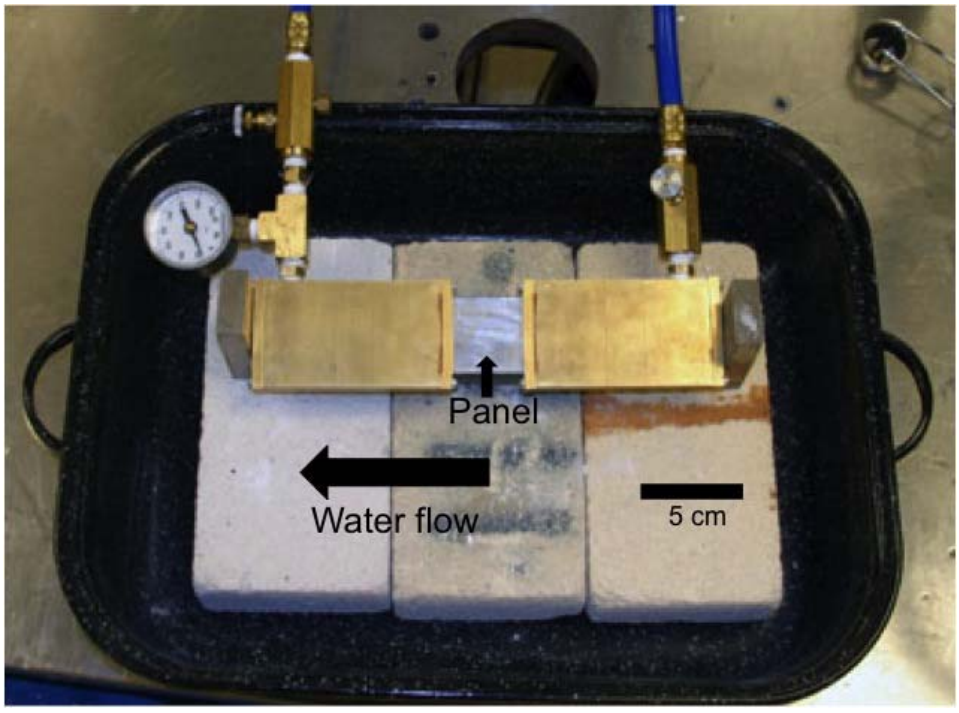

Figure 2.2: Image of the high-temperature testing apparatus for the actively-cooled thermostructural panel.

The water traveled through a brass fixture designed to produce a fully developed turbulent flow before entering the panel. The exact replication of the model would

require channel pressures up to 0.9 MPa and a flow rate of 90.5 cm^3/s. However, the capabilities of the facility limited the flow rate and pressure ranges available. Pressures could range from 0.035 to 0.4 MPa with flow rates up to 80 cm^3/s.

Rerunning the panel failure model with the available conditions, it was possible to find an alternative channel pressure and flow rate combination that predicted a similar failure mode as the original conditions of tensile failure in the center of a cooling channel. In order to reduce the possibility of boiling the water in the cooling channels, the maximum available pressure was used for the panel testing of 0.4 MPa. A flow rate of 16 cm^3/s was used to achieve the maximum use temperature on the surface of the panel. Both the as-fabricated and strengthened panels were subjected to similar temperatures, pressures and flow rates to determine the relative performance of the panels. The comparision parameters include the maximum temperature of the hot side, the maximum pressure and minimum flow rate.

2.9.2 Temperature and Measurements

In order to measure the comparison parameters, which included the maximum surface temperature, thermocouples were attached to the heated side of the panel. The performances of the as-fabricated and strengthened panels were compared to each other and to model predictions.

2.9.3 Pressure and Water Flow Measurements

Replicating the failure conditions in the model required control of the water pressure and flow rate. The pressure of the water in the actively-cooled channels was measured with a dial gauge and the water flow was measured with a flow meter. The city water pressure available was 0.4 MPa. The water flow could be varied with a pair of needle valves, one located at the inlet and one located at the outlet in order to achieve a similar failure mode as predicted in the panel geometry model.

Chapter 3

Vapor Phase Strengthening Feasibility

The feasibility of a vapor phase strengthening approach was established on small scale samples before applying the process to a fabricated sandwich panel. The following sections describe the results of experiments performed to determine if this approach was a possible solution for strengthening refractory-lean nickel-base alloys in a post-fabricated state.

3.1 Aluminization

The aluminization time and temperature used for the feasibility studies was one hour at 950 °C based on aluminization studies performed by Dunand et al. [18]. As described below, the results for four alloys were investigated using similar aluminization conditions. No effort was made to achieve a particular aluminum concentration, the objective was investigating the feasibility of establishing a γ - γ' microstructure without any other detrimental phases.

SEM inspection as well as concentration profiles from WDS of the as-aluminized alloys revealed high aluminum concentration layers on the outer surfaces of all the samples. The number of phases present, thicknesses and aluminum concentration of the layers varied from alloy to alloy. There was no appreciable change in total sample thicknesses for any of the alloys investigated. For example, on average after aluminization, the IN-625 sample thickness changed from 201 to 203.8 μm, an increase of only 1.9%. The concentration profiles of the samples, compared with the Ni-Cr-Al ternary phase diagram [48] and thermodynamic calculations were used to identify the phases present.

3.1.1 Haynes X-750

The as-aluminized coating on the H-X750 alloy had two layers, the outermost consisting of a mixture of Al_3Ni_2 and β-NiAl and with a β-NiAl innermost layer. The thickness of the outermost layer was 90 μm and the inner layer was 30 μm. Figure 3.1 shows the as-aluminized microstructures and the associated concentration profiles for the H-X750 alloy in the as-aluminized condition.

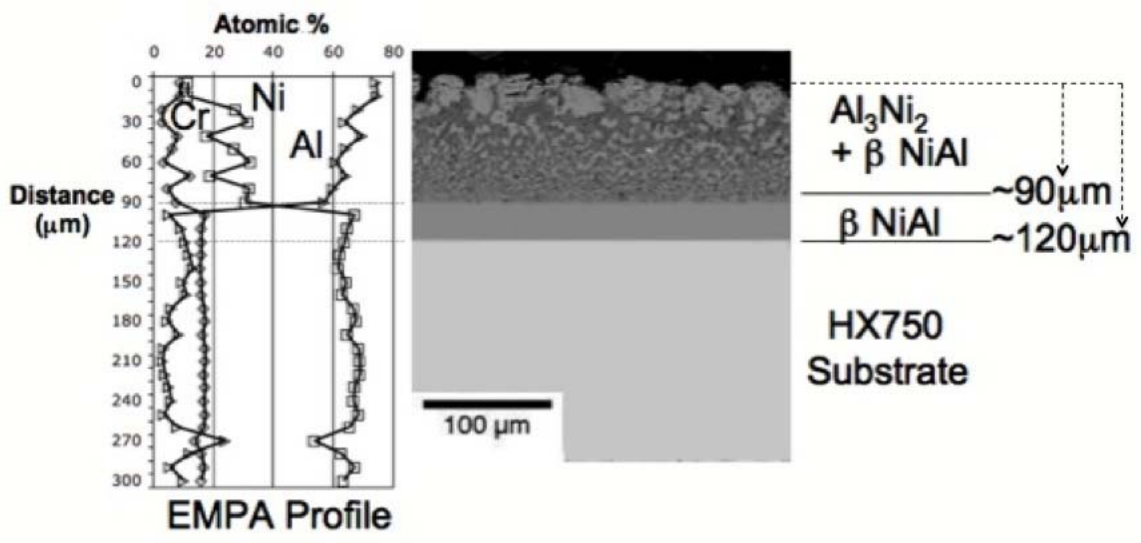

Figure 3.1: BSE image and EMPA concentration profiles of as-aluminized X-750

3.1.2 Haynes 214

The H-214 alloy had a very similar as-aluminized microstructure compared to the H-X750 alloy, with the only variation being a thicker coating. The two layers present consisted of Al_3Ni_2 and β-NiAl (outer layer) and β-NiAl (inner layer). The Al_3Ni_2 + β-NiAl layer was 180 μm thick while the β-NiAl layer had a thickness of 20 μm. Figure 3.2 shows the microstructure and associated concentration profiles for the as-aluminized alloy 214.

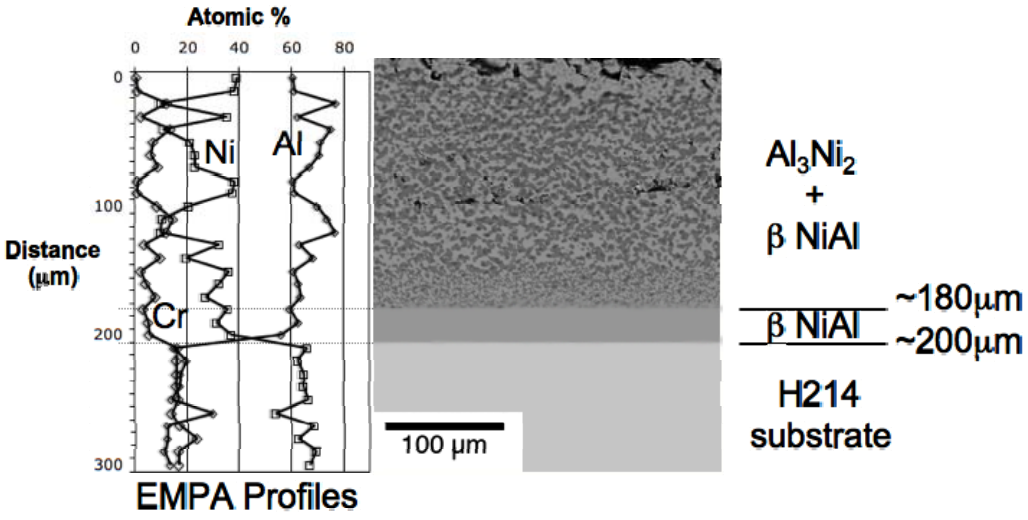

Figure 3.2: BSE image and EMPA concentration profiles of as-aluminized 214.

3.1.3 Inconel 625

The IN-625 alloy showed the most complex microstructure with an outer two-phase layer near the surface, measuring approximately 25 μm thick and a second 10 μm subsurface layer consisting of a third phase. The topmost layer of the aluminized specimen contained the highest concentration of aluminum throughout the sample. The cross section of the IN-625 sample is shown in Figure 3.3a. The concentration profiles of the aluminized surface (Fig. 3.3b) compared with thermodynamic predictions of phase equilibria reveal that the topmost layer consists of α-Cr and β-NiAl while the inter-layer is α-Cr, γ-Ni and the topologically close packed (TCP) sigma (σ) phase. In addition, X-ray scans of the post-aluminized sample showed new peaks consistent with the sigma phase.

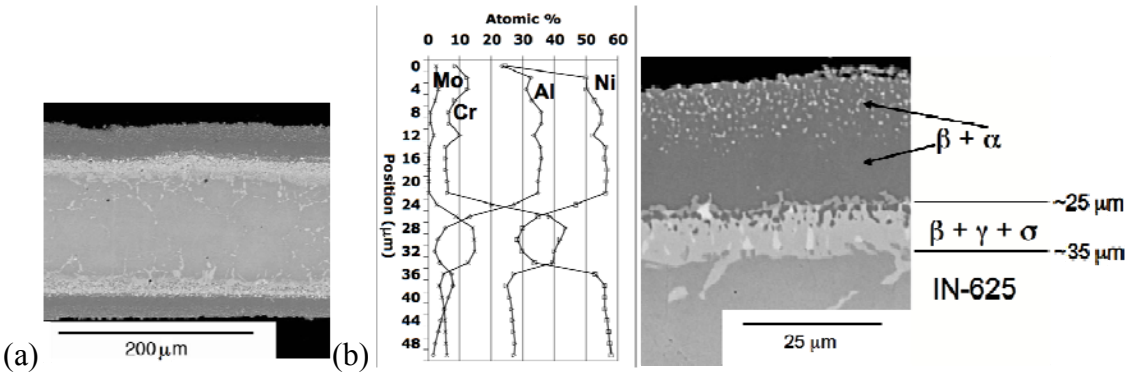

Figure 3.3:(a) BSE image of cross section of as-aluminized IN-625. (b) Concentration profile for as-aluminized 625 specimen.

3.1.4 Inconel 693

The as-aluminized microstructure of the IN-693 alloy also consisted of three layers. The outermost layer consisted of the two phases α-Cr and β-NiAl, with a thickness of 30 μm. The middle layer, with a thickness of approximately 3 μm, consisted of the three phases α-Cr, β-NiAl and γ. The innermost layer was also three phases and with the decreased aluminum concentration consisted of α-Cr, γ and γ′ with a thickness of 5 μm. The SEM images and EMPA concentration profiles are shown in Figure 3.4.

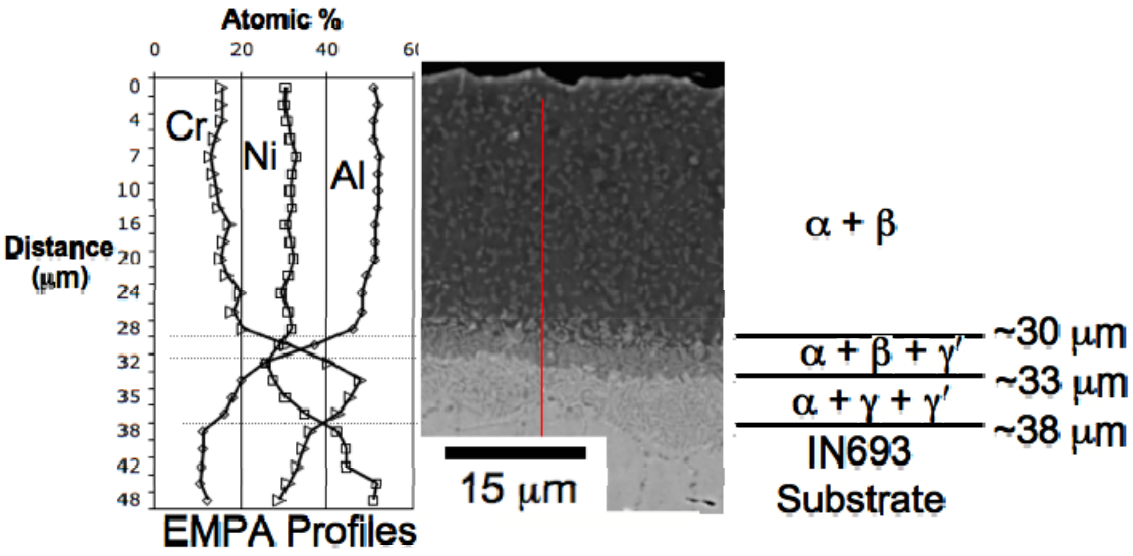

Figure 3.4: BSE image and EMPA concentration profiles of as-aluminized 693.

3.2 Homogenization

Initial homogenization studies utilized a homogenization heat treatment of 118 h at 1050 °C for the IN-625 samples while the remaining alloys were heat treated for 150 h at 1100 °C. The selection of the times and temperatures is discussed in Section 3.5.2. The availability of the IN-625 alloy samples with a thickness of 200 μm allowed for the reduced homogenization time.

3.2.1 Haynes X-750

A piece of the H-X750 sheet was ground to a thickness of 400 μm to determine if the aluminum deposited on both surfaces was able to diffuse to create a sample homogenized

through the thickness. This sample was aluminized for 1 hour at 950 °C and annealed for 150 hours at 1100 °C. Concentration profiles from EMPA and SEM images confirmed diffusion of aluminum after annealing from the initial coatings through the thickness of the H-X750 sheet. In Figure 3.5 the aluminum concentration profile indicates an aluminum concentration of approximately 4.5 weight percent. This is an increase from the 0.8 weight percent in the as-received X-750 alloy. Thermodynamic calculations were also employed to determine pseudo phase diagrams for all the alloys investigated at the homogenization temperature. The implications of these diagrams will be discussed in Section 3.5.2. Although not investigated in this study, X-750 has small $M_{23}C_6$ carbides up to 50 nm in diameter to control grain size during rolling [49].

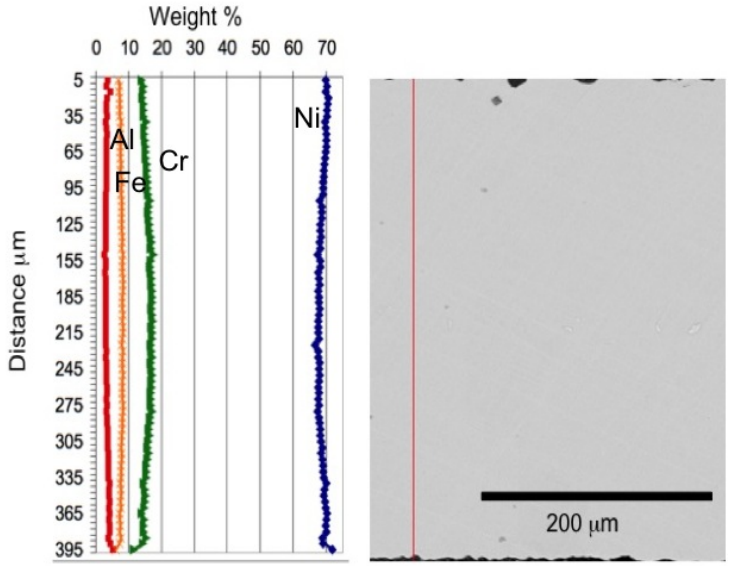

Figure 3.5: BSE image and EMPA concentration profiles of X-750 alloy aluminized for 1 hour at 950 °C and annealed for 150 hours at 1100 °C.

3.2.2 Haynes 214

The 214 alloy sample was over 1 mm in thickness and therefore the preliminary aluminization of 1 hour at 950 °C and the homogenization treatment of 150 hours at 1100 °C was unable to completely homogenize the aluminum as with the H-X750 alloy described above. From the concentration profiles and SEM images (Figure 3.6) it is clear that the H-214 alloy showed increased aluminum concentration to a depth of approximately 250 μm from the coated surface at the bottom. Unlike the X-750 alloy, H-214 maintained an outer layer consisting of β + γ + γ′ and an inner layer of γ + γ′ following homogenization.

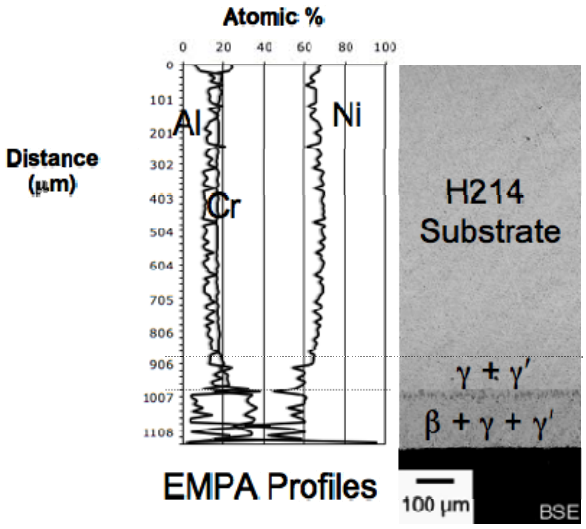

Figure 3.6: BSE image and EMPA concentration profiles of 214 alloy aluminized for 1 hour at 950 °C and annealed for 150 hours at 1100 °C.

3.2.3 Inconel 625

The IN-625 sample (Fig. 3.7) aluminized for 1 hour at 950 °C and homogenized for 118 hours at 1100 °C showed a relatively uniform microstructure. The concentration profiles from WDS indicate the aluminum has diffused through the thickness of the sample while leaving the TCP σ phase in the region where the second layer of the aluminized coating was originally located. In addition, large σ precipitates formed at the grain boundaries during the homogenization treatment, Figure 3.7.

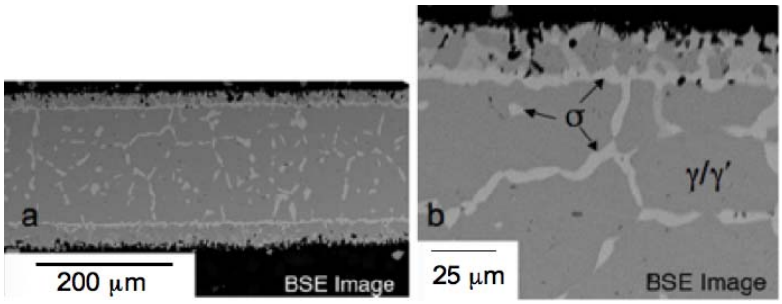

Figure 3.7: BSE images of 625 alloy aluminized for 1 hour at 950 °C and annealed for 118 hours at 1100 °C. (a) Cross section view showing the homogenization through entire thickness. (b) Higher magnification image to show σ precipitates at grain boundaries.

3.2.4 Inconel 693

The IN-693 alloy contains much more chromium than the other alloys investigated in this study, which ultimately affected the stability of the γ′ phase. The 693 alloy sample (Figure 3.8) aluminized for 1 hour at 950 °C and annealed for 150 hours at 1100 °C

showed an increase in aluminum concentration to a depth of 250 μm. There was a residual β coating remaining on the surface with α-Cr particles present to the depth of aluminum penetration.

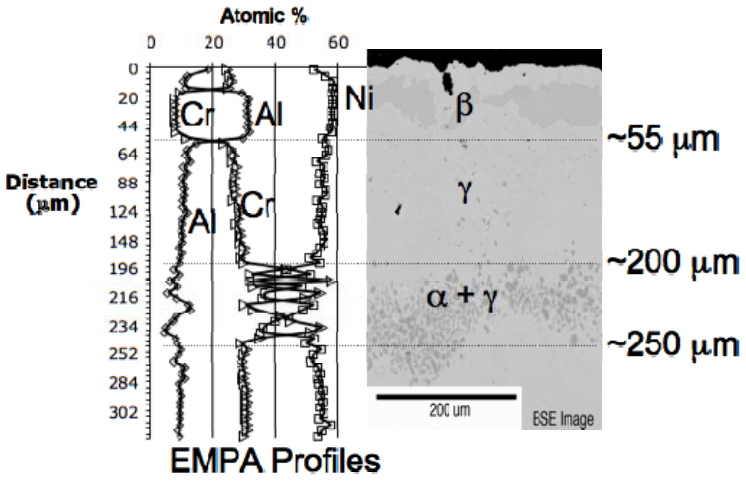

Figure 3.8: BSE image and EMPA concentration profiles of 693 alloy aluminized for 1 hour at 950 °C and annealed for 150 hours at 1100 °C.

3.2.5 Precipitation of the γ′ phase

To check for the presence of γ′ precipitates in the processed samples, the etched surfaces were examined and secondary electron (SE) images were taken. All of the alloys investigated had increased aluminum concentrations to depths up to 250 μm. However the IN-693 sample did not achieve sufficient increase in concentration to precipitate γ′. All of the other alloys showed a fine precipitate microstructure in the γ matrix as shown

in Figure 3.9. These precipitates resulted from cooling the samples from the homogenization temperature and not from aging treatments.

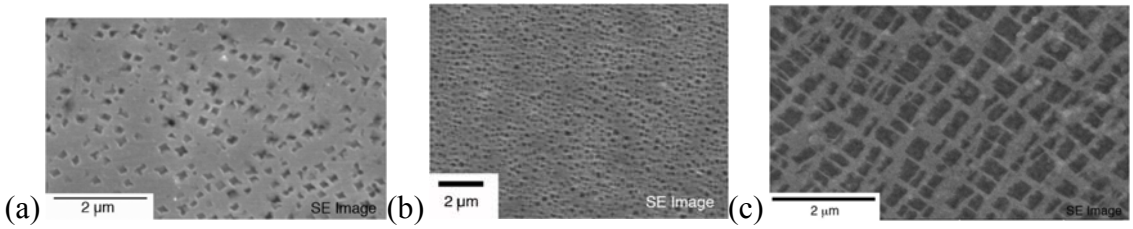

Figure 3.9: SE images of aluminized and annealed samples. Etched to reveal microstructure (a) 625 grain interior (b) 214 and (c) X-750

In the grain interior of alloy IN-625 (Figure 3.9a), the precipitates were approximately 150 – 200 nm in diameter. Both alloy H-214 and H-X750 (Figure 3.9b and 3.9c) contained precipitates 100 – 150 nm in diameter.

3.3 Hardness Testing

The hardness of the samples was measured as a function of position through the thickness of the aluminized + homogenized samples. Alloy IN-625 showed an increase from 197 ± 12 Hv in the as-received condition to 403 ± 46 Hv in the processed condition through its thickness, as the sheet was thin enough to be uniformly enriched in aluminum. For the remaining alloys it was necessary to use samples with greater thicknesses, as thinner sheets were not available in small quantities. In these alloys there was a correlation between the hardness and aluminum penetration through the thickness. Although the

thickness of the sheets used was greater than the aluminum penetration, homogenization would still be possible with standard thinner sheets.

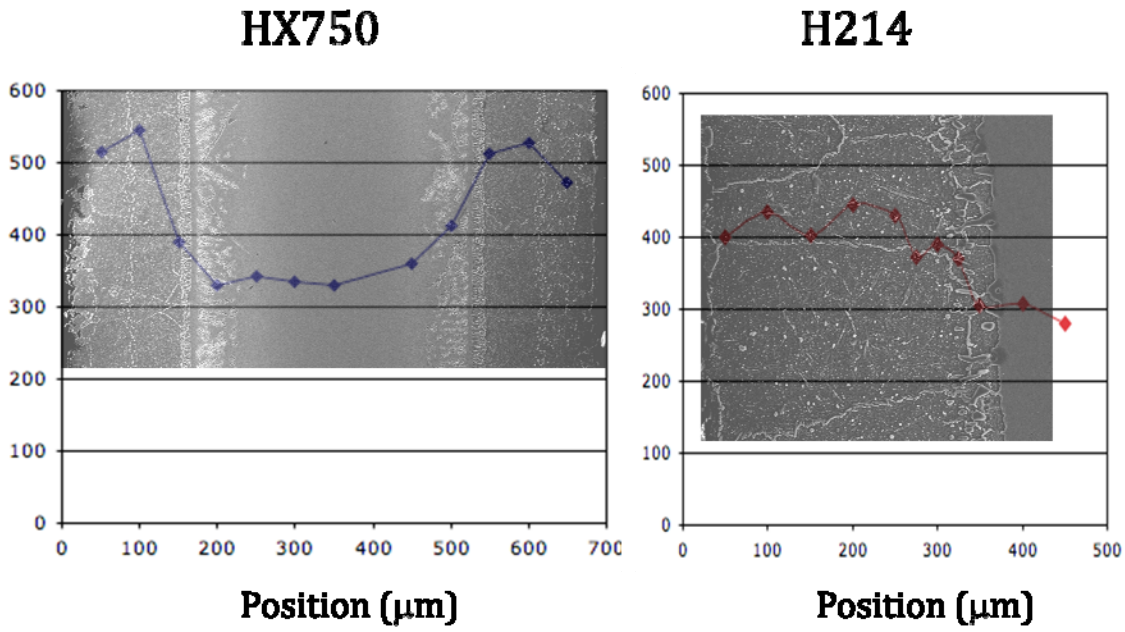

Figure 3.10: Measured Vickers hardness as a function of depth on X-750 and 214 samples aluminized for 1 hour at 950 °C and annealed for 150 hours at 1100 °C.

Figure 3.10 shows the measured hardness as a function of position over a representative etched image of the H-214 and H-X750 samples for easy comparison of hardness to microstructure. As mentioned in Section 3.2.1, the X-750 sample shown was ground to a thickness of 0.4 mm while the sample in Figure 3.10 was 0.7 mm thick and therefore was not completely homogenized. It is apparent that the hardness is higher near the edges of the samples and falls off past the depth of aluminum penetration. As the aluminum diffuses into the samples, the aluminum concentration is higher near the surfaces of the samples in Figure 3.10, which increases the volume fraction of the γ' phase in

equilibrium. With the increase in hardness near the surface of the samples, it can be inferred that there is a correlation between hardness and an increase in volume fraction of γ′. On average, the change in hardness from the bulk as-received material to near the edge of the processed samples was 326 ± 19 to 445 ± 20 for H-214 and 204 ± 9 to 550 ± 32 Hv for H-X750. A summary of the averaged hardness values for all the alloys is given in Table 3.1.

Table 3.1: Vickers hardness for as-received and aluminized + homogenized alloys

Alloy	As-received	Aluminized + Homogenized
IN-625	197 ± 12	403 ± 46
IN-693	297 ± 27	497 ± 30
H-214	326 ± 19	445 ± 20
H-X750	204 ± 9	550 ± 32

3.4 Oxidation Behavior

All as-received alloys and processed samples were subjected to oxidation in air for 1 hour at 1000 °C. After homogenization, there was a residual β coating remaining at the surface of all of the samples except for H-X750. Even without the β coating (which should improve the oxidation properties of the material [48]), all the alloys including H-X750 showed improved oxidation resistance.

All the as-received alloys grew a thick, irregular mixed oxide layer while the aluminized and annealed samples grew a thinner, more uniform oxide layer. Of all the alloys, IN-625 showed the largest reduction of oxide thickness, from approximately 170 μm for the

as-received material to 6 μm in the processed sample (Figure 3.11). The remaining alloys showed very consistent oxidation behavior with the IN-693 images being representative (Figure 3.12). There was close to one order of magnitude reduction in oxide layer thickness.

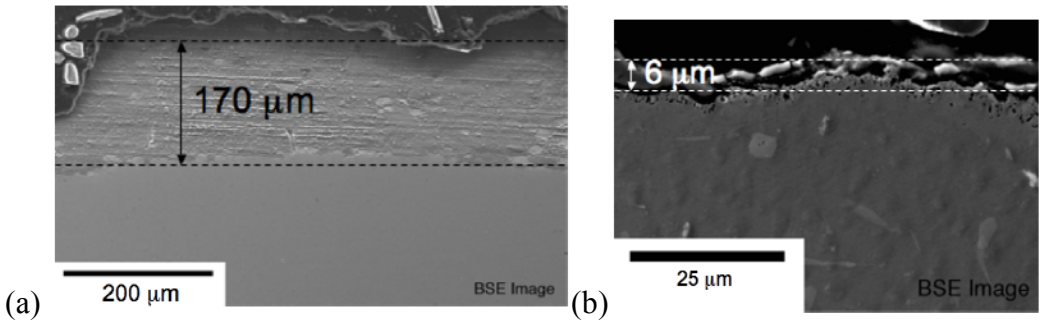

Figure 3.11: Oxidation layer formed on 625 after 1 hour at 1000 ºC. (a) As-received 625. (b) 625 aluminized for 1 hour at 950 °C and annealed for 118 hours at 1100 °C.

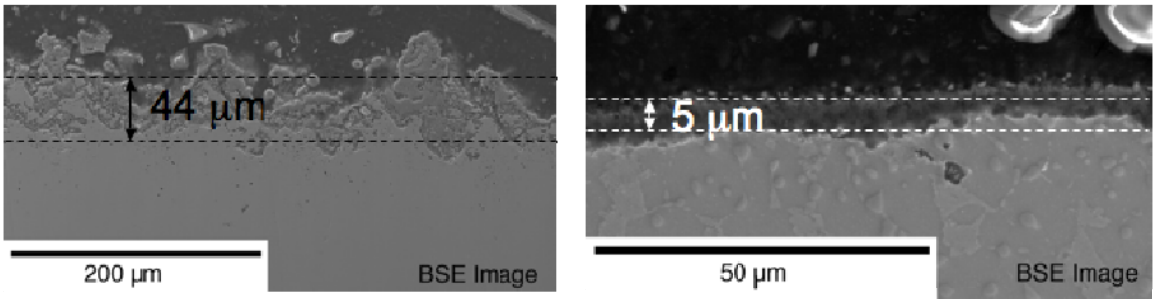

Figure 3.12: Oxidation layer formed on 693 after 1 hour at 1000 °C. (a) As-received 693. (b) 693 aluminized for 1 hour at 950 °C and annealed for 150 hours at 1100 °C.

3.5 Discussion

3.5.1 Deposition of Source Aluminum

In this study the feasibility of strengthening solid solution nickel-based alloys in a post-fabricated state has been addressed. For this processing approach to be feasible for use in thermostructural panels, where geometry must be closely controlled, it is important that the sheet thicknesses remain nominally unchanged through the procedure. After the aluminization of all the alloys, it was shown that the nominal thickness of the samples remained consistent with the samples that were not aluminized, which indicates primarily inward aluminum diffusion during the process, typical with high-activity pack aluminization [27].

Although each alloy experienced the same aluminization process, the depth of aluminum penetration as well as phases present varied with each alloy. Both the microstructural and diffusion differences are due to the differences in major alloying elements of these alloys. Different elements will promote stability of certain undesirable phases, specifically TCP σ and α-Cr in this study. For IN-625, the presence of Mo as an alloying component makes it possible to form the σ phase [9,10]. The IN-693 alloy contained more Cr than the other alloys, and due to the limited solubility of Cr in NiAl phases [51] a precipitation front rich in Cr formed at the interface as will be discussed further. Importantly, as shown in Figure 3.13, thermodynamic databases for Ni-based systems are

becoming sufficiently mature that the diffusion path and phases formed could be evaluated as part of the sheet material selection process.

The differences in major alloying elements will substantially affect the interdiffusion constants of a system [13]. The increased Cr in IN-693 inhibited the inward diffusion of Al, decreasing the depth of the aluminized coating. The increased Cr showed α-Cr phase stability, which can interfere with the growth rate of the coating [52]. The increased Mo content of IN-625 reduced the depth of the aluminized coating, consistent with the lower mobility of Mo [53]. The difference in thickness of the aluminized layer for the alloys H-214 and H-X750 is due to the Nb present in H-X750. The lower mobility of Nb and other refractory additions found in superalloys will decrease the coating thickness [53]. Also, alloy H-214 already contains the most Al of all the alloys investigated, making less additional Al necessary for stability of the aluminum-rich Ni_3Al phase.

3.5.2 Thermodynamic and Kinetic Considerations

Once the aluminum has been added to the samples, an annealing treatment is required to homogenize the aluminum concentration within 10 atomic percent of the mean aluminum concentration through the thickness of the thinnest sample (IN-625) of 200 μm. The homogenization time required was estimated using a Fourier series approximation modeled for a composite slab and including the initial conditions consistent with this study [13].

$$C(x,t) - C_{ave} + (C_{coat} - C_{ave}) \exp\left[\frac{-\pi^2 D t}{l^2}\right] \quad (1)$$

Where C_{ave} is the average aluminum concentration over the entire thickness, C_{coat} is the aluminum concentration in coating, D, the interdiffusion coefficient, and *l* being half the thickness of the sample. Interdiffusion data for β-NiAl [54] and nickel solid solutions [55] were considered in calculating an estimate for the required annealing time. An interdiffusion coefficient of D = 3.68 x 10^{-15} m^2/sec at 1100 °C was used to approximate an annealing time of 118 hours for a sheet thickness of 200 μm. Examination of IN-625 after this annealing treatment by WDS confirmed that the aluminum concentration was homogenized through the 200 μm thick sample as in Figure 3.7.

The aluminum addition to the H-X750 and H-214 alloys resulted in a γ + γ′ microstructure after the homogenization treatment. The other alloys contained either a σ phase (IN-625) or the α-Cr phase (IN-693). For comparison, the calculated Ni-Cr-Al pseudo ternary phase diagrams for each alloy are shown in Figure 3.13 at the homogenization temperature of 1100 °C. These phase diagrams were calculated keeping the minor alloying elements constant for each alloy and varying the Ni, Al, and Cr concentrations.

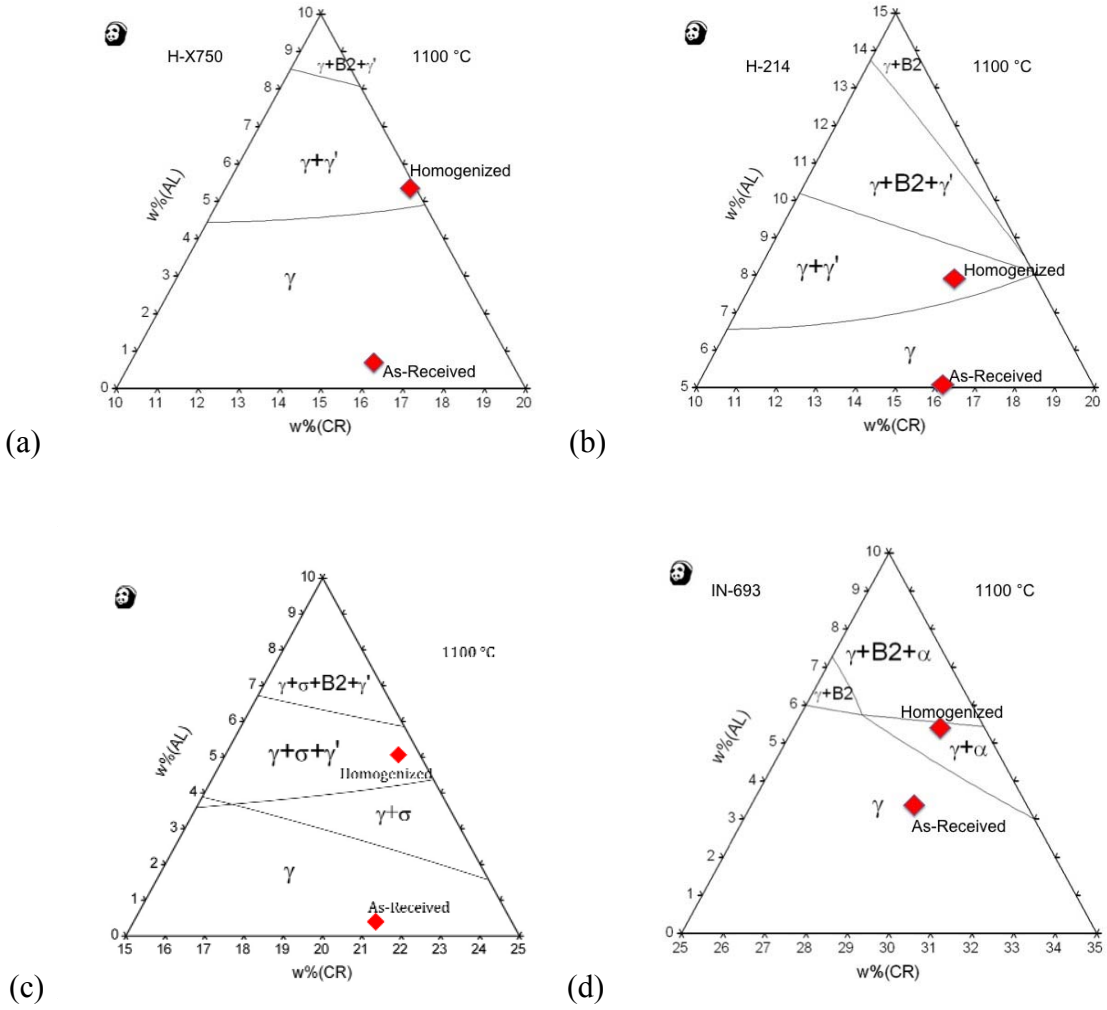

Figure 3.13 Thermodynamically calculated Ni-Al-Cr pseudo ternaries for the alloys tested showing the initial as-received alloy composition and the composition after the aluminization and homogenization treatments. (a) H-X750 (b) H-214 (c) IN-625 (d) IN-693.

The IN-625 alloy showed large σ phase precipitates after the homogenization, as reported above. The precipitation of the TCP σ phase is common after long exposure at elevated temperatures of Ni-based superalloys containing high concentrations of chromium and molybdenum [9,10]. Padant^{TM} computational analysis confirmed the stability of γ + γ′ + σ at 1100 °C for the new alloy composition.

After homogenization, IN-625 was somewhat embrittled, fracturing when bent through a large radius. Foils of the other alloys were still deformable following homogenization. The brittleness of the TCP σ phase that was present at the grain boundaries will reduce the ductility of the alloy [9,10]. It is possible to avoid this phase by choosing an alloy containing less molybdenum, as shown with the other alloys tested in this study.

The IN-693 alloy had the largest chromium content of all the alloys tested. Due to the increased Cr, the alloy preferentially stabilized α-Cr as opposed to γ′ within the γ matrix. From the ternary calculated in Figure 3.13, it is clear that the new alloy composition falls into the γ + α phase field.

3.5.3 Post-Strengthened Properties

Microhardness testing was performed to gain insight into the strengthening that occurred in the alloys due to the processing they underwent. Hardness can be used to infer the yield strength [56] and therefore is an easy and fast way to get feedback on changes in mechanical properties.

Hardness testing was used in the feasibility portion of this study as a means to show that the processing improved the strengthening of the alloys. From this data it was possible to choose an alloy to investigate further. Due to the largest increase in hardness, alloy H-X750 was determined to be the most promising alloy for the application.

Similar to the hardness testing, the simple oxidation test was used to show the feasibility of the process and the potential improvements. All of the alloys showed improved oxidation resistance when comparing the as-received to the processed samples.

The reduction of oxide growth was achieved with the increase of aluminum at the surface of the alloys. After the homogenization procedure, the surface microstructure of the alloys was near or contained the β NiAl phase. When exposed to oxygen at high temperatures, the β phase will form an Al_2O_3 oxide layer [57]. Alumina is a protective oxide [57] in that it will not grow uncontrollably and spall. The addition of aluminum in the alloys, especially having larger concentrations at the surface, ensures the formation of alumina opposed to a mixed oxide that grew on the as-received samples.

3.6 Summary

The purpose of these initial tests was to determine the feasibility of the vapor phase strengthening process. It was not initially clear that this approach would be thermodynamically possible in a reasonable time frame. Initial aluminization and homogenization studies demonstrate that:

- All alloys have improved oxidation resistance as well as an increase in hardness. The reasonable time frame and improved properties make this a feasible process.

- The pack cementation process resulted in an aluminum rich outer coating on all alloys tested while maintaining the geometrical dimensions of the samples within 2%. This was possible due to the high activity of the aluminization pack, which results in primarily inward diffusion of aluminum. The microstructures of the coatings were consistent with previous literature and thermodynamic databases.

- A homogenization treatment of 150 hours at 1100 °C showed aluminum penetration up to a depth of 250 μm. This would allow for the processing of a 0.5 mm thick sheet in approximately 7 days. Although the length of time needed is not ideal, it is not prohibitively long.

- Although the aluminum was able to penetrate all of the alloys to a significant depth, it was clear that not all of the alloys were appropriate for this application. For example, the IN-625 alloy formed the topologically close packed phase σ during the aluminization process, which continued to precipitate and grow during the homogenization treatment. The formation of this phase greatly reduces its ductility, making it unsuitable for this process. The IN-693 alloy also proved to unsuitable for this process. During the homogenization, the added aluminum preferentially stabilized α-Cr rather than the desired γ′ phase. Although no deleterious phases were formed, the phases present in equilibrium after processing were not desired for this application.

- Both H-214 alloy and H-X750 alloys contained no undesirable phases after the homogenization treatment. Combining this with the increased hardness and improved oxidation properties, the vapor phase strengthening process is valid for these alloys. The H-X750 alloy was chosen for further investigation because of its large increase in post-processing hardness – an increase of almost 170%.

Chapter 4

Integrated Modeling

As mentioned in Chapter 2, three models were used in an integrated manner to determine the combination of material properties and processing parameters that result in a thermostructural panel with minimum weight. The models include the Pandat^{TM} software for thermodynamic modeling, a yield strength model developed by Kozar et al. [17] and a minimum weight panel geometry optimization developed by Vermaak et al. [32]. Each of the models will be discussed in more detail in the following sections and the integration of the models will also be discussed further.

4.1 Thermodynamic Modeling

As discussed in previous chapters, the aluminide coating deposited on the surface of the alloys will not be used for its traditionally intended purpose. Instead of providing environmental protection, the coating is used as an aluminum source for the bulk alloy. This process results in a new alloy composition with additional aluminum.

With the new alloy composition comes new alloy phases and associated stable phase composition ranges. Fortunately, advanced thermodynamic modeling programs that alleviate the need to determine the phase stability and composition ranges experimentally are available. In this study the thermodynamic modeling and calculations were done with Pandat™ that uses the CompuTherm databases.

Pandat allows for all alloy components to be accounted for and generates phase diagrams based on thermodynamic modeling of individual phases that may develop within the multi-component system. As discussed in 3.5.2 and shown in Figure 3.13 (repeated below in Figure 4.1), ternary phase diagrams were calculated for all the alloys for fixed levels of base alloying elements and varying aluminum, chromium, and nickel. Although the base alloying elements vary slightly across the thickness in the post-processed state, those changes result in negligible changes in the stable phases predicted.

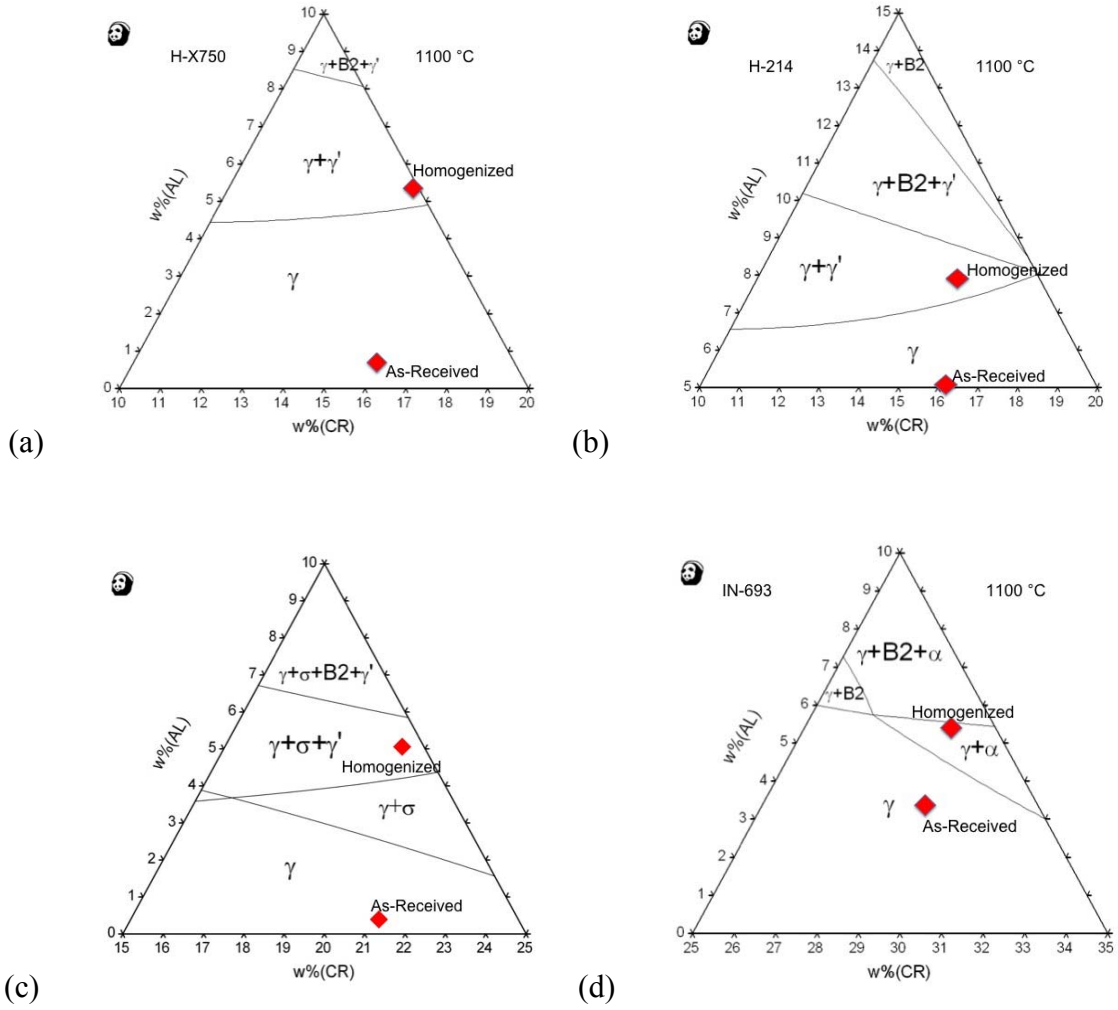

Figure 4.1 Thermodynamically calculated Ni-Al-Cr pseudo ternaries for the alloys tested showing the initial as-received alloy composition and the composition after the aluminization and homogenization treatments. (a) H-X750 (b) H-214 (c) IN-625 (d) IN-693.

In addition to calculating phase diagrams over a range of composition, it is possible to calculate the volume fractions of phases at specific temperatures and compositions. This is very useful when determining potential heat treatment temperatures for a multi-sized population of precipitates.

Although the thermodynamic modeling cannot determine the optimum microstructure, it is a very useful tool in determining the necessary level of aluminum required to achieve the desired volume fraction of γ′. Thermodynamic modeling is utilized by calculating if achieving a given microstructure is thermodynamically possible with available chemistry and potential heat treatments. It should be noted that not all thermodynamically calculated databases predict the correct equilibrium phases and volume fractions. However, due to the extensive validation of the databases for this class of Ni alloys, the CompuTherm database is reasonably accurate [58-60].

4.2 Yield Strength Modeling

For a particular alloy composition, the microstructure will have a large impact on the yield strength [9,10]. In order to eliminate the need to fabricate, heat treat and test individual alloys and microstructure variants, a yield strength model has been developed by Kozar et al. [17] for nickel-based alloys. This model calculates the potential increase in yield strength due to the following strengthening mechanisms: solid solution, weak pair coupling, strong pair coupling, and grain boundary strengthening. The input variables for the model include the composition of the matrix and precipitates, grain size, total volume fraction of γ′ precipitates as well as up to three distinct precipitate populations. Although the yield strength model allows for any number of microstructure combinations, it does not consider if the microstructures are thermodynamically feasible, it will only show what is mechanically ideal.

For this research, the model was exercised for a range of precipitate sizes, distributions and volume fractions for microstructures with two populations of precipitates. The larger population was varied from 100 – 200 nm while the smaller population was varied from 20 – 35 nm with full results listed in the Appendix. From these results, typically the higher yield strengths corresponded to microstructures containing 40-55 volume percent γ' with relatively small precipitate sizes, typically 100 – 120 nm for the larger population. Depending on the specific total volume fraction and relative volume fractions of the two distributions, the most favorable smaller precipitate size ranged from 20 to 35 nm. An example of the output from the yield strength model calculated for a microstructure with a total of 40 volume percent γ' (20 % at 110 nm and 20 % at 25 nm) is shown in Figure 4.2a) with the contributions from each strengthening mechanism in Figure 4.2b). It should be noted that the predicted yield strength is much larger than would typically be expected and this discrepancy will be discussed further in Section 4.5.

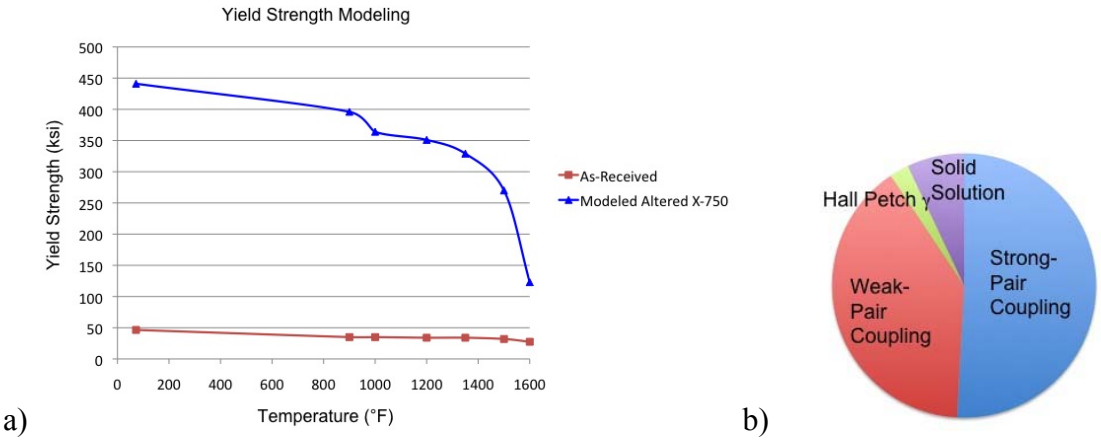

Figure 4.2: a) Maximum predicted increase in yield strength calculated for a precipitation strengthened altered X-750 base alloy with a total of 40 volume percent γ′ (20 % at 110 nm and 20 % at 25 nm) b) Relative contributions from each strengthening mechanism.

Although the particular sizes mentioned above were for the highest yield strength at room temperature, when taking the temperature dependence into account, there were additional microstructures that could be considered favorable due to better potential performance at higher temperatures with increased volume fraction γ′. Also, it was necessary to confirm that the proposed microstructures were thermodynamically feasible. Furthermore, achieving such high strength levels would require confirmation that deformation mechanisms predicted in the strength model are actually operative. The panel geometry modeling will make it possible to assess the performance of each feasible microstructure in terms of panel weight.

4.3 Panel Geometry Modeling

The planned application for this research is a thermosturctural panel for use in the combustor of a scramjet engine. As discussed in Chapter 1, actively-cooled sandwich panels would be an appropriate structure for such an application. Vermaak et al [32] have developed an analytical model that embodies the results of a large set of finite element calculations and functions to optimize the geometry of a rectangular channeled/actively-cooled panel for minimum weight. Weight was chosen as the optimizing parameter as it is arguably the most important parameter for a flight application.

The model considers both the thermal and mechanical stresses experienced by the panel and will only return a geometry optimized for minimum weight if the panel is able to survive the environment. Therefore, the thermomechanical loads on the panel dictate the optimum geometry for the thermostructural panels. In addition to simply calculating if a panel will survive, the anticipated failure mode and loading contributions are calculated along with the ratio of the calculated value to the failure criterion, showing how close the panel is to a certain failure mode. Although this information is extremely useful, the model is only designed to calculate the stresses for steady-state conditions. Therefore, if a panel is near failure under a certain stress, it is possible for the panel to fail with a slight change in the environment.

The model takes material property inputs and determines the optimum geometry for a range of cooling liquid flow and heat transfer conditions of the panel. The full list of material properties include: density, coefficient of thermal expansion, Young's modulus, conductivity, Poisson's ratio, maximum use temperature, reference yield strength (yield strength at 127 °C), and the yield strength change with temperature. The material properties that were varied included reference yield strength, yield strength as a function of temperature, and maximum use temperatures. Table 4.1 includes the values for the material properties that were held constant for the optimizations.

Table 4.1: Values of material properties considered constant for this application.

Density	8276 [kg/m^3]
Coefficient of Thermal Expansion	16.0 x 10^{-6} [1/K]
Young's Modulus	128 x 10^9 [Pa]
Conductivity	23.0 [W/mK]
Poisson's Ratio	0.30

This model allows for accurate comparison between materials because it optimizes the panel geometry for each material separately. For example, Figure 4.3 [32] shows the weight of a variety of optimized rectangular channeled panels as a function of the equivalence ratio. The equivalence ratio is the ratio of the fuel flow necessary for cooling to the fuel needed for combustion therefore an equivalence ratio of 1 means all the fuel needed for cooling will be used for combustion where a ratio of 1.5 means that for cooling, it is necessary to carry 1.5 times the fuel needed for combustion.

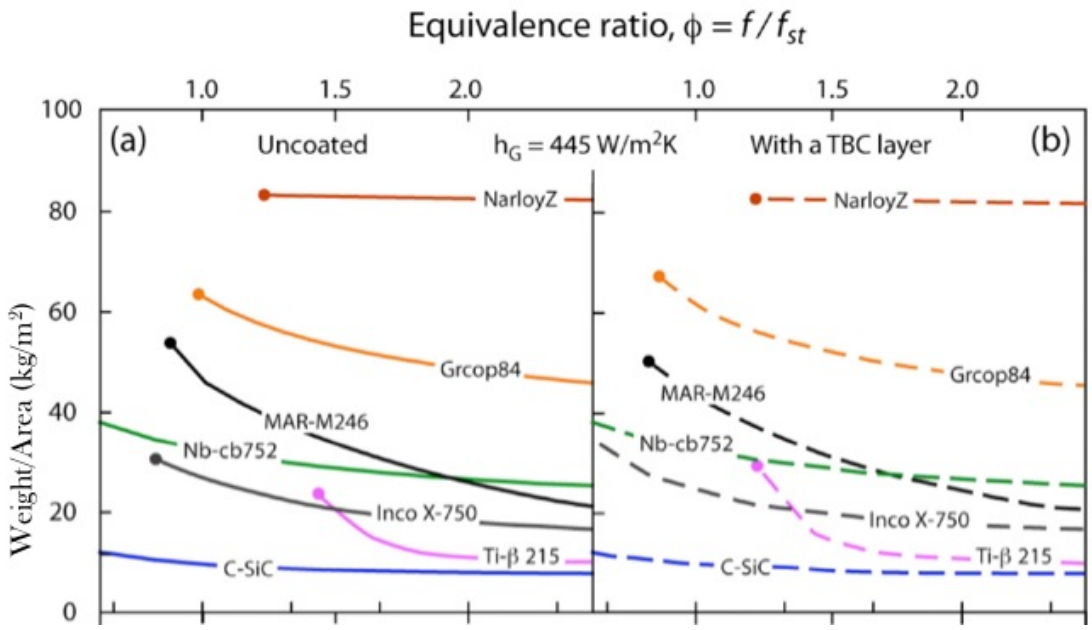

Figure 4.3 Geometrically optimized thermostructural panels for minimum weight for a variety of materials from Vermaak et al. [32].

This model is advantageous because of its ability to compare material systems with consideration of the full set of material properties that are relevant to panel operating conditions. For example, copper alloys (such as Grcop84 in Figure 4.3) may be considered for their conductivity, but the model demonstrates that their relatively low yield strength requires extra material to sustain the required loads making the panel prohibitively heavy. The titanium alloy would also be considered for its low density, however the extra fuel needed for cooling makes it a less obvious choice. It should be noted that the maximum use temperature for the alloys chosen by Vermaak et al. [32] are overly aggressive therefore the mass versus equivalence ratio curve for the X-750 alloy reported in Section 4.4 will be slightly altered due to a more conservative T^* value.

From Figure 4.3 it appears that the C-SiC material is the most promising from a weight standpoint. Unfortunately, the low toughness, oxidation resistance and high cost of the material are concerns. Considering that the panel is designed for the interior of a combustor with airspeed above the speed of sound, it is crucial to have a material that has high enough toughness to tolerate damage by ingestion of foreign objects. For example, engulfing raindrops at those speeds would cause serious erosion problems with a material such as C-SiC [61].

In order for metallic systems to compete with a C-SiC panel, the material properties must be improved. However, due to the complex relationships between material properties and the optimized geometry, the connection between a reduced overall weight and specific material properties is not easily determined. Although the exact connections cannot be determined, Vermaak et al [32] considered the effects of increasing two parameters on the optimized weight of a panel: the reference yield strength, S, and the maximum use temperature, T^*, above which the mechanical properties drop off precipitously. The resulting flow rate versus mass is shown in Figure 4.4 with the gray area indicating the solution region of the as-received material and the colored area indicating the solution region for a 25% increase in yield strength (green) and a 25% increase in T^* (orange).

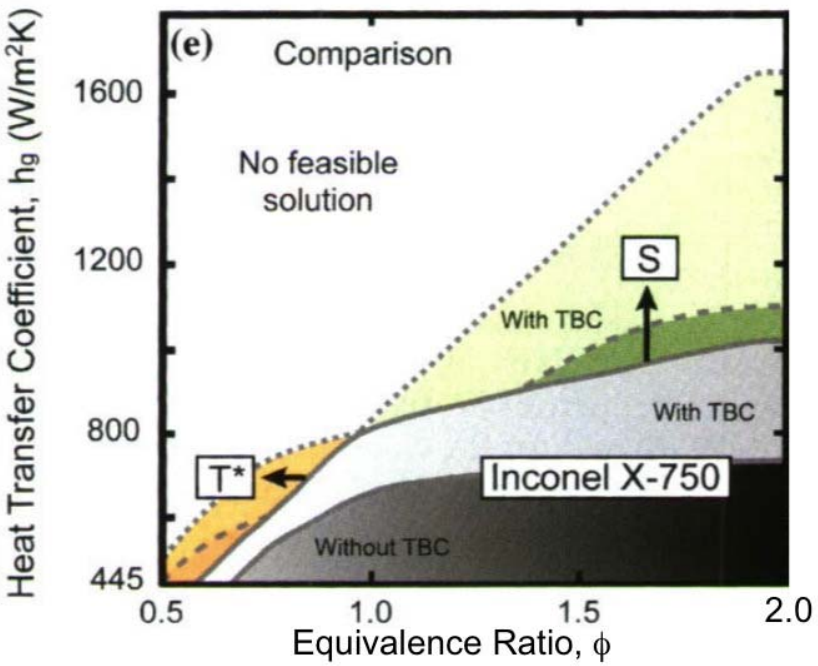

Figure 4.4: Increase in feasible solution space for the X-750 alloy by increasing the reference yield strength, S, and the maximum use temperature, T^*, by 25% from Vermaak et al. [32].

From Figure 4.4, which considers X-750, it appears that increasing the reference yield strength has a larger effect than increasing the maximum use temperature. However, increasing T^* permits lower fuel flow rates. This investigation was performed for a range of heat transfer coefficients and therefore may not be directly translated for a reduced mass for a given heat transfer coefficient. Although this investigation gave some insight into the relative importance of which mechanical properties to improve, the integration of the three models is necessary to achieve a panel with the global minimum weight.

4.4 Integrating Models

As mentioned above, the panel geometry model will optimize a panel based on a set of material properties. It is not clear exactly what combination of material properties will result in the optimized panel. If a microstructure were chosen using the thermodynamic and yield strength modeling, it would be possible to find an optimum geometry *for that microstructure*. However, in order to find the microstructure corresponding to a rectangular channeled thermostructural panel with the global minimum mass all the models need to be used in an integrated manner.

To begin, the Pandat^{TM} software was used to calculate a pseudo phase diagram for the base X-750 alloy at the homogenization temperature of 1100 °C. All elemental concentrations besides Ni, Al and Cr where held constant at the as-received values as the small variants of the minor alloying elements proved to be insignificant. Figure 4.5 shows this pseudo phase diagram with the following values for the minor alloying elements (in wt%): Fe = 7.8, Ti = 2.4, and Nb = 0.9.

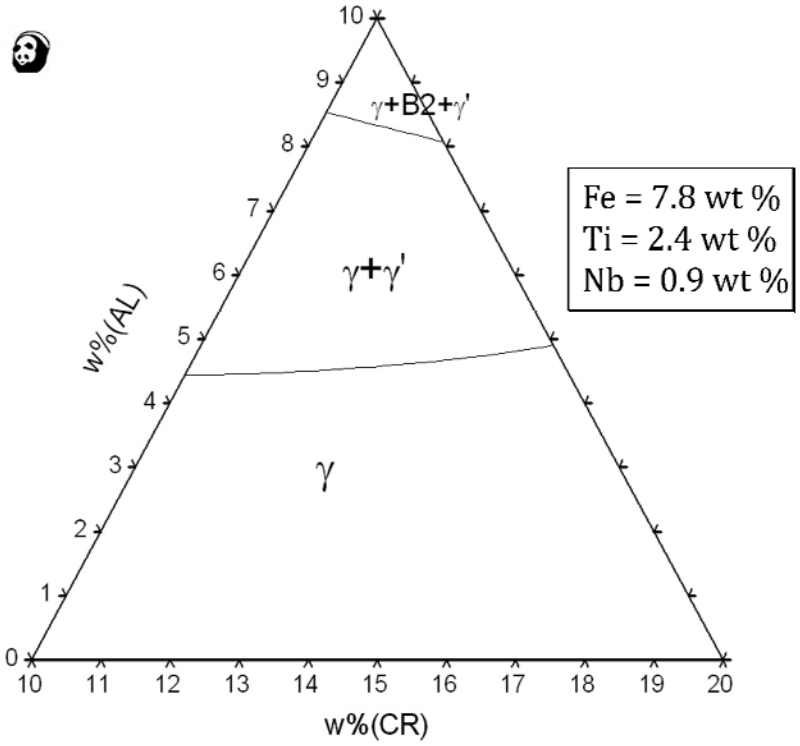

Figure 4.5: Pseudo phase diagram calculated with Pandat^{TM} software for the X-750 alloy varying Ni, Al and Cr.

As discussed in section 4.2, the yield strength model was used to determine promising microstructures and the corresponding yield strengths versus temperature were calculated. The temperature dependent yield strength and maximum use temperature from those microstructures were put into the panel geometry model and mass versus equivalence ratio was calculated. A three-population microstructure similar to commercial disc alloys was also included for comparison. The results of those calculations are plotted in Figure 4.6.

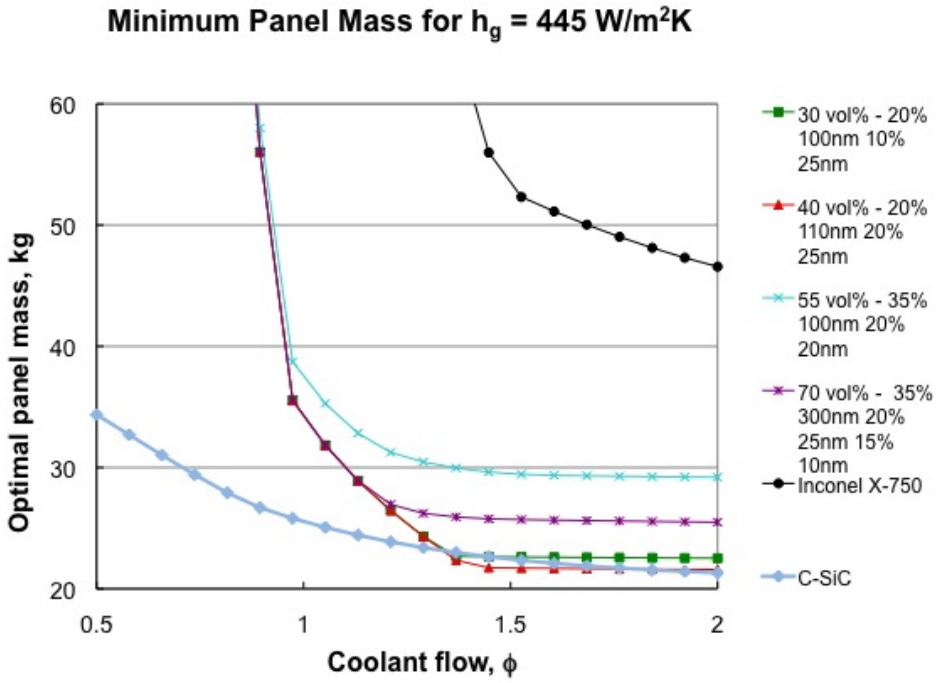

Figure 4.6 Optimized panel mass versus equivalence ratio based on the material properties calculated with the yield strength model for the most promising microstructures.

From the plot it is clear that the improvement in material properties from the X-750 alloy have reduced the mass of a metallic thermostructural panel to be competitive with a C-SiC for equivalence ratios as low as 1.25. Compared to the as-received X-750 alloy, the panel mass with a modeled microstructure has been reduced by approximately 50% for a given equivalence ratio, or cooling flow rate. The promising microstructures are in the range from 30 to 70 volume percent γ'. The proposed alloys with 40-50 volume percent precipitates showed the most potential in terms of weight reduction (Appendix).

From the integrated modeling it appears that a microstructure with a volume fraction of γ′ of approximately 40 with the populations evenly distributed between 110 nm and 25 nm is desirable. An average of 4.6 wt% aluminum is necessary to achieve the desired microstructure. The resulting optimized geometry of the rectangular channeled panel consisted of channels with dimensions of 8 mm x 5 mm and wall/face sheet thicknesses of 0.4 mm. In order to check microstructures at and around this target, multiple heat treatments were employed for the tensile samples. Results of these tests will be discussed in Chapter 5.

4.5 Discussion

Calculations performed by integrating the models indicate that an intermediate volume fraction of fine-scale precipitates show the most promise for a minimum panel mass. The yield strength model predicted that intermediate ranges of volume percent precipitates would have higher yield strengths. As mentioned in Section 4.2, the calculated room temperature yield strength is well above a value that is typical for a nickel based alloy. Although it is clear that γ′ precipitates will strengthen the alloy, the outputs from this model may not accurately predict realistic values. The model predicted that the smaller population strengthened with a weak pair mechanism while the larger precipitate population strengthened with a strong pair mechanism. The model assumes a Gaussian distribution of sizes for each population of precipitates. It is most likely that with a combination of both strong and weak pair mechanisms at work, the model has over estimated the possible increase in yield strength.

Considering the thermostructural panel optimizations, there are some general trends relating improvement in mechanical properties to improvements in panel performance. From the investigations into the specific effects of increasing maximum use temperature and increasing the reference yield strength, it appears that increasing the maximum use temperature will yield lower equivalence ratios for a given mass while increasing the yield strength will reduce the mass for a given equivalence ratio. The yield strength model indicated favorable microstructures concerning high room temperature yield strength. Although the general trends of increasing yield strength and maximum use temperature were described above, it is not obvious if one is particularly better than the other or what combination of the two result in the most efficient structure.

4.6 Summary

A combination of thermodynamic, yield strength and geometric modeling was necessary for global optimization of the geometry for a minimum mass thermostructural panel. Considering this process:

- The yield strength and geometric models were integrated to identify the range of microstructures that result in a global minimum panel mass while the thermodynamic modeling was used to confirm the feasibility of the microstructures. Without the integration, it would only be possible to find minimum masses for a given microstructure with no insight into if that

microstructure actually produces an optimized thermostructural panel of if it was thermodynamically possible.

- A range of precipitate volume fraction and sizes were investigated for definition of microstructures that would yield low mass panels. A microstructure consisting of a total 40 vol % γ' (20 vol % at 110 nm and 20 vol % at 25 nm) was determined to result in an optimized rectangular channeled panel with channel dimensions of 8 mm x 5 mm with wall and face sheet thicknesses of 0.4 mm.

- These integrated models showed that, although not intuitive, a strengthened nickel-base alloy could be competitive from a weight standpoint with a C-SiC panel. Although extra fuel would need to be carried, having a metallic combustor could reduce the potential for fracture in the case of foreign object damage.

Chapter 5

Vapor Phase Strengthening of X-750

Although Chapter 4 discussed the modeling that was employed to determine a goal microstructure, it is still necessary to demonstrate vapor phase strengthening of the X-750 alloy and experimentally measure the resulting mechanical properties. Also, the heat treatment temperatures and aging times must be developed and validated. The following sections will discuss the experimental results of the strengthened X-750 alloy with the goal microstructure.

5.1 Aging Treatments

The optimized microstructure determined in Chapter 4 consisted of a total of 40 volume percent γ′ with 20 percent at a size of 110 nm and 20 percent at 25 nm, which correlates to an aluminum concentration of 4.6 weight perent. The thermodynamic feasibility of this microstructure was confirmed with Pandat^{TM} and was used to determine the solution temperature and aging treatment temperatures. A solution treatment of one hour was carried out at 1200 °C. According to the thermodynamic calculations, 20 volume percent γ′ is stable at 1075 °C. The elemental concentrations of the matrix were used to

determine an additional aging temperature of 980 °C to precipitate another 20 volume percent γ′ at the lower temperature. Due to the phase stability of γ + γ′ (shown in Figure 5.1) it is possible to increase the equilibrium volume fraction of γ′ by aging at lower temperatures.

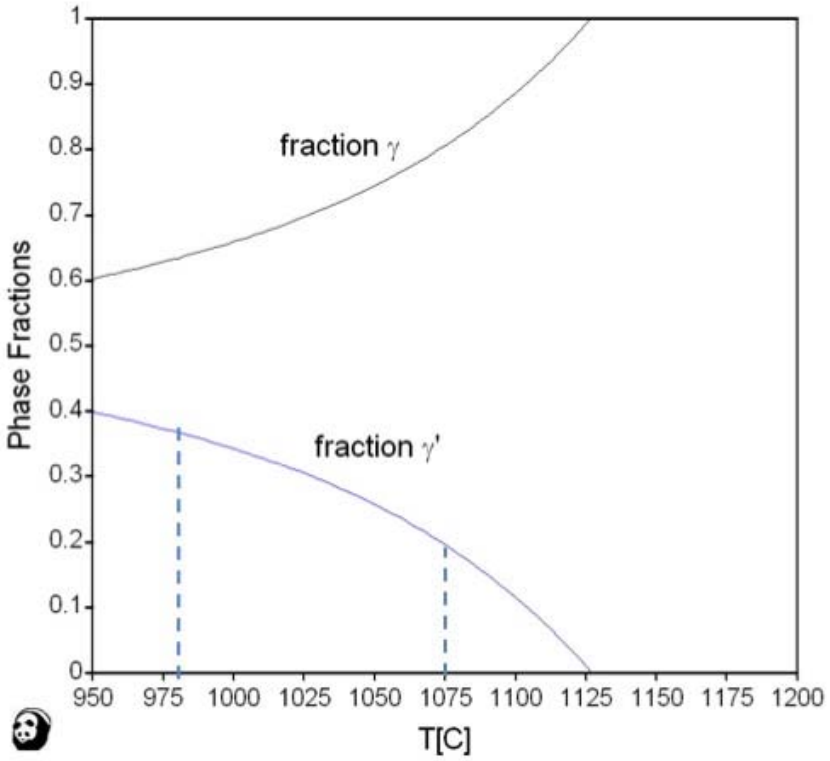

Figure 5.1: Volume fraction of phases in equilibrium for an altered X-750 alloy containing 4.6 weight percent aluminum calculated with Pandat™ software.

As mentioned above, the precipitate sizes are rather small and therefore require relatively short heat treatments. The equation for Ostwald Ripening below [15] was used to

determine the approximate aging time to achieve precipitate populations with sizes of 110 nm and 25 nm.

$$r^3 - r_o^3 = kt \qquad [2]$$

Extrapolating a value for k of 1.19×10^{-24} m^3/s for 1075 °C and 1.77×10^{-25} m^3/s for 980 °C from an experimentally determined k value for an alloy with similar aluminum and chromium content to X-750 [62], the required aging times to obtain two populations of precipitates of 110 nm and 20 nm were estimated to be 16 minutes at 1075 °C and 2 minutes at 980 °C. Due to the approximate nature of the kinetic constant k, aging treatments were carried out for a range of times, 13 to 19 minutes and 2 to 5 minutes respectively. Although these short aging times are not ideal, considering the maximum surface temperature before failure predicted by the panel code is 875 °C, the higher final aging temperature makes the microstructure more stable at the maximum use temperature.

In order to achieve these very short aging treatments, an environmentally controlled vertical tube furnace with the ability to quickly move the sample from the hot zone to the cool zone was used. The cool zone of the furnace remained at temperatures no greater than 250 °C throughout the treatments. After a solution treatment at 1200 °C the samples were rapidly cooled at a rate of approximately 50 °C/s to inhibit precipitation of γ′ during cooling. The aging treatments were carried out by initially heating the furnace to the desired temperature and then lowering the samples into the hot zone. When the

necessary time had elapsed, the samples were pulled from the hot zone and rapidly cooled at approximately 50 °C/s. Samples were etched with an electrolytic etching solution of 11% H_3PO_4, 45.5% H_2SO_4 and 43.5% HNO_3 to dissolve the γ matrix while leaving the γ′ phase exposed on the surface. This allowed for inspection of the precipitate size and morphology. SEM images of the γ′ precipitates resulting from the heat treatments are shown in Figure 5.2.

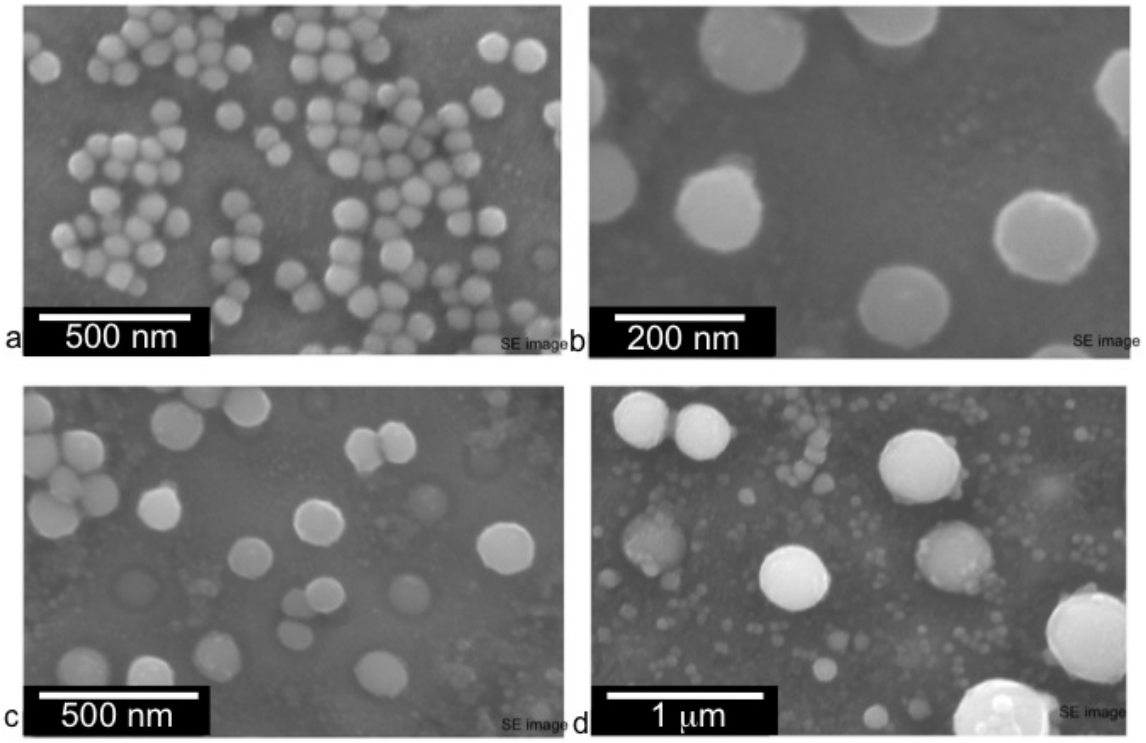

Figure 5.2: SEM secondary electron images of the γ′ precipitates in altered X-750 alloy with 4.6 weight percent aluminum with the following aging treatments: a) 13 minutes at 1075 °C and 2 minutes at 980 °C. b) 15 minutes at 1075 °C and 2 minutes at 980 °C. c) 17 minutes at 1075 °C and 3 minutes at 980 °C. d) 19 minutes at 1075 °C and 5 minutes at 980 °C.

Although the images have different magnification scales, the average precipitate size increases from image a to image d. All of the aging treatments appeared to produce spherical precipitates. The shortest aging treatment of 13 minutes at 1075 °C resulted in precipitates approximately 90 nm in diameter while the longest treatment of 19 minutes had precipitate sizes of approximately 400 nm. The 15 minute aging treatment at 1075 °C appeared to result in the precipitates closest in size to the goal of 110 nm. Although difficult to image, the smaller precipitates from the second aging treatment are visible especially in Figure 5.2d. The sample in Figure 5.2d had a 5 minute aging treatment at 980 °C. The other samples had between 2 and 3 minute aging treatments which resulted in precipitates between approximately 20 and 35 nm.

5.2 Tensile Tests

As discussed in the previous section, a range of heat treatments was carried out and hardness measurements were performed. In addition to the hardness tests, flat sheet tensile dogbone samples were prepared and tested. The single sample tensile tests were performed at room temperature to compare with the yield strength model. As mentioned above a range of heat treatments were employed to target the goal microstructure. Table 5.1 contains the measured yield strength, ultimate tensile strength and strain at fracture for as-received and strengthened samples.

Table 5.1: Tensile properties measured and calculated from single tensile tests for as-received X-750 alloy and altered X-750 alloy with 4.6 weight % aluminum with varying two stage aging treatments.

Sample	Yield Strength (MPa)	Ultimate Tensile Strength (MPa)	Strain at fracture (%)
As-Received	260	745	28.5
13 min @ 1075 °C 2 min @ 980 °C	887	918	1.2
15 min @ 1075 °C 2 min @ 980 °C	879	941	2.7
17 min @ 1075 °C 3 min @ 980 °C	724	740	0.7
19 min @ 1075 °C 5 min @ 980 °C	630	705	1.8

Based on these tests, the improvement in yield strength varied from approximately 240% to 340% depending on the heat treatment while the strain at fracture has been reduced by at least an order of magnitude. There appears to be a trend when comparing the calculated yield strength and the heat treatment times. As the heat treatment time increases, the room temperature yield strength decreases. The shorter aging times correlate to smaller precipitate sizes. Although the 13 and 15 minute aging treatments yielded similar results, the 17 and 19 minute heat treatments had considerable reductions in strength.

Compared to the as-received X-750 the strengthened tensile samples exhibited a considerable reduction in ductility. With a higher strength material a reduction in ductility would be expected, but in this case another mechanism also contributed. Upon further examination of the samples after fracture, a large number of surface cracks were

apparent along the gauge length. For these samples, a residual β-NiAl coating was left on the surfaces of the samples after annealing. Although this residual coating improves the oxidation resistance of the samples, the brittle nature of the β layer can initiate surface cracks [60]. The small cracks along the surface of the tensile samples (see Figure 5.3) may be in part responsible for the ductility reduction. Beyond this, lower ductility would generally be expected for a higher strength material.

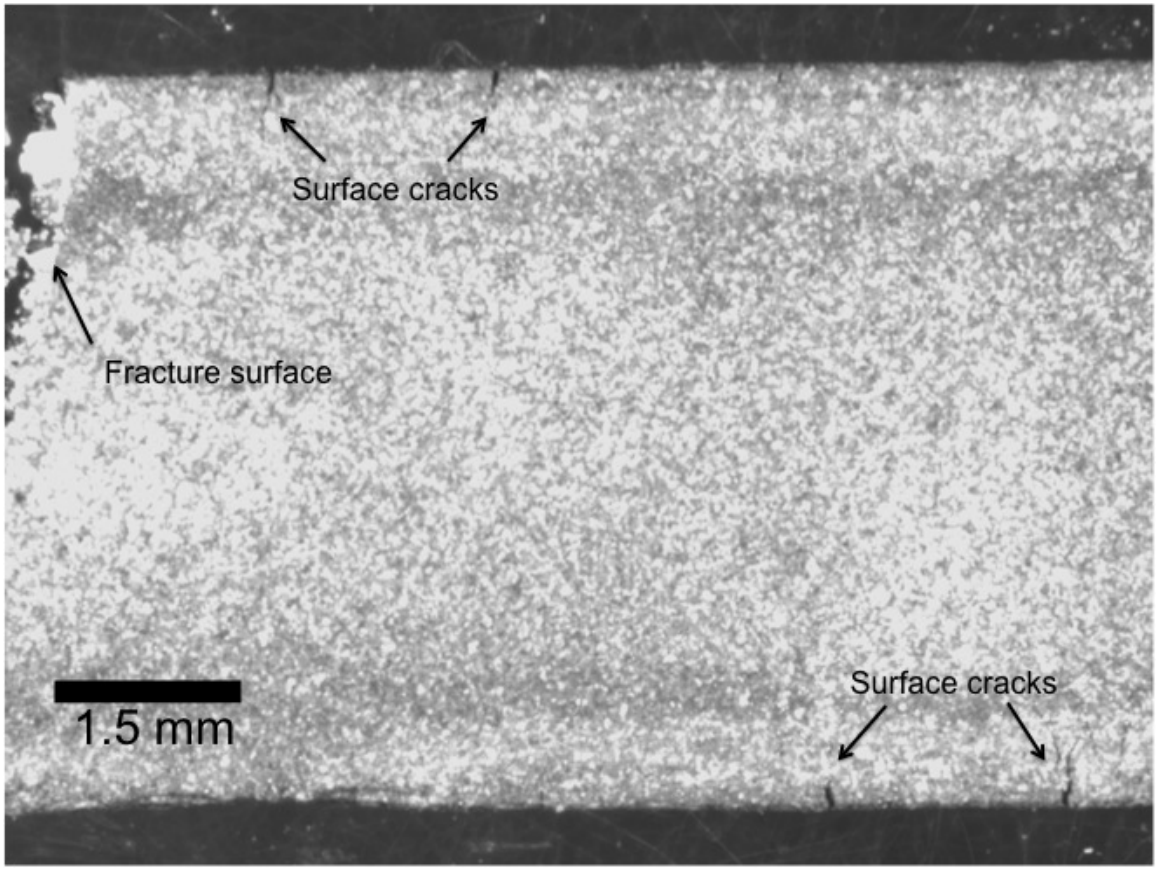

Figure 5.3: Optical microscope image of the gauge section of a tensile sample after fracture showing the crack initiation sites along the surface.

5.3 Discussion

The results from the room temperature tensile tests show strengthening of the as-homogenized panel due to aging at 1075 °C between 13 and 15 minutes. In the yield strength model, when the size of the larger population of precipitates is increased, there is a significant decrease in the strong-pair coupling contribution. As discussed in Section 1.2.2, the optimum strengthening due to precipitates occurs at the intersection of the relative strength due to strong and weak pair coupling mechanisms. The room temperature tensile results show that the longer aging times appear to be past the precipitate size that produces the highest yield strength.

Although the strains at fracture were significantly smaller for the vapor phase strengthened samples, most are still significantly larger than a 3-D woven C-SiC structure, which is approximately 0.6% [64]. The purpose of this study is demonstrating the feasibility of a metallic thermostructural panel to be competitive with a C-SiC panel. At the optimal aging treatments, the vapor phase strengthened alloy has approximately 450% more ductility than the C-SiC. As mentioned above, the brittle nature of the β phase on the surface of the samples reduced the ductility of the tensile samples as well as provided crack initiation sites. Although this study showed the strengthened X-750 alloy had as much as a 450% increase in ductility over C-SiC, it is possible to improve the ductility even further without the β phase layer present. Longer annealing treatments could be used to eliminate the β phase, diffusing all of the source aluminum into the bulk of the alloy.

Even when using the most ideal mechanical properties experimentally measured, the values determined experimentally fell far short of the values predicted by the yield strength model. It should be noted that the model predicts the *maximum* possible increase in strength and as shown in Figure 4.2b) (repeated here in Figure 5.4), slightly over 90% of the strengthening comes from strong and weak pair coupling. As discussed in Section 4.5, the model predicts that the smaller precipitates strengthen with a weak pair mechanism while the larger precipitates strengthen with a strong pair mechanism. It is most likely that with a combination of both strong and weak pair mechanisms at work, the model has over estimated the possible increase in yield strength. Also, the combination of a brittle surface layer and not fully realizing the predicted incremental strength from each strengthening mechanisms reduced the overall yield strength from the calculated value of the model.

Figure 5.4: Percentage of modeled strengthening occurring from specific mechanisms.

5.4 Summary

Mechanical tests of samples subjected to aluminization, homogenization and subsequent solutioning and aging have been conducted. Experimentally determined values with those calculated from the models discussed in Chapter 4 showed the following results:

- Aging treatments were developed to produce a microstructure with 40 total volume fraction γ′ consisting of two distinct populations of 20 volume fraction at approximately 110 nm and 20 volume fraction at approximately 25 nm. From extrapolation of experimental values, the microstructure can be made with a 14 minute aging treatment at 1075 °C followed by a 2.25 minute aging treatment at 980 °C.

- Tensile tests demonstrate increased yield strength in the vapor phase strengthened samples. Even with a brittle β phase layer on the surface of the samples, the room temperature tensile tests showed a 340% increase in yield strength and 2.7% ductility.

Chapter 6

Thermostructural Panel Tests

The previous chapters have demonstrated the feasibility of the vapor phase strengthening. However, it is still necessary to fabricate and strengthen rectangular channeled thermostructural panels. The strengthening process applied to the panels is discussed below as well as the high temperature performance of the heated panels with active cooling.

6.1 As-Fabricated Panels

Although the feasibility of the panel strengthening process was demonstrated in Chapter 3, it is further necessary to consider the feasibility of fabricating a rectangular channeled panel. Although the methods described in the following sections are not the only means to fabricate a rectangular channeled panel, two methods, brazing and electrodischarge machining, were investigated for this study. The feasibility was initially tested with a brazed panel before the determination of the optimized geometry.

6.1.1 Brazed Panel

A rectangular channeled sandwich panel was fabricated by brazing X-750 alloy sheets with AMDRY DF-6A. The top and bottom surfaces were brazed together with evenly spaced webbing perpendicular to the face sheets to create the channels. The face sheets and panel webbing were 0.635 mm thick creating 9 channels with dimensions 5.1 x 8.8 mm The geometry of the panel was accomplished by placing the braze tape on the ends of the webbing and using a reusable fixture to hold the pieces in place during the brazing process. The cross section of the sandwich panel is shown in Figure 6.1a and there was good joint integrity between the X-750 pieces, shown in Figure 6.1b.

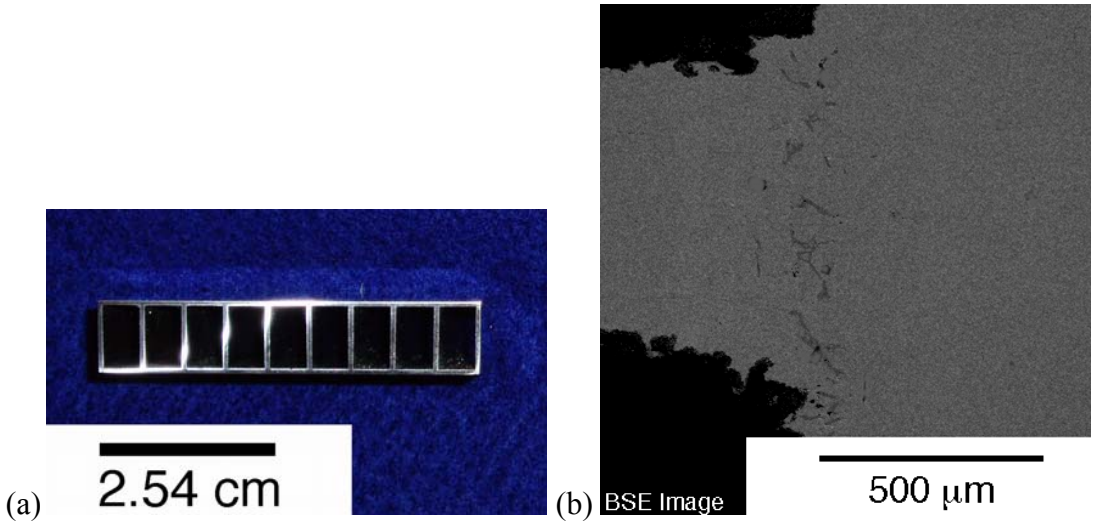

Figure 6.1: (a) Cross section of rectangular channeled panel fabricated from X-750 alloy sheet (b) SEM image of brazed joint

The brazing was performed with a pair of heat treatments, 20 minutes at 450 °C (to remove organics from the braze tape) and 30 minutes at 1200 °C to join the pieces. These are standard specifications [41] without the annealing treatment on the panels after brazing. However, after brazing and aluminization, the panels were subjected to a long annealing heat treatment, which is sufficient to homogenize the aluminum concentration. Comparing the homogenization of the joint and the aluminum homogenization, the longer process is the diffusion of the aluminum through the thickness of the samples. This allows the annealing step of the brazing process to be eliminated.

6.1.2 Electric Discharge Machined Panel

Due to the inability to order small quantities of the X-750 alloy sheet in thicknesses less than 0.635 mm, an alternative method was needed to fabricate a panel with the optimized geometry calculated from integrated modeling. Beginning with a solid 6.35 mm thick plate of X-750 alloy, the plate was traditionally milled to appropriate exterior dimensions of 5.8 x 45 x 63.5 mm and 8 x 5 mm channels were cut along the length of the panel using an electric discharge machining process. This left a rectangular channeled panel with webbing and face sheet thickness of 0.4 mm, as shown in Figure 6.2.

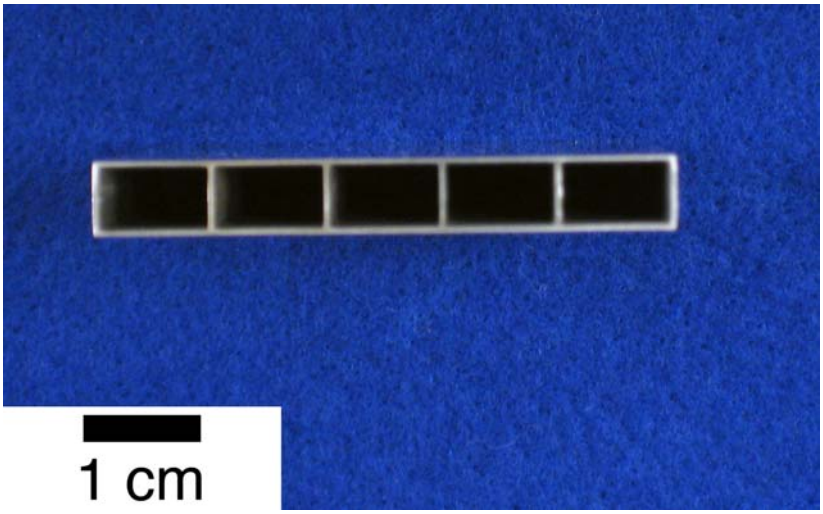

Figure 6.2: Image of the cross section of the electric discharge machined panel with webbing thickness of 0.4 mm.

6.2 As-Aluminized Panels

In order to more clearly refer to the fabricated panels, the following designations will be used and are summarized in Table 6.1. Panel 1 will refer to the brazed panel described in Section 6.1.1 while panel 2 will refer to the EDM fabricated panel described in 6.1.2. If the panel was altered in any way after fabrication, either the letter A or H will follow it representing aluminized and homogenized respectively. The specific aluminization and annealing conditions are described in Table 6.1.

Table 6.1: Designations referring to fabricated X-750 alloy panels and alterations to those panels.

Designation	Description
Panel 1	Panel fabricated by brazing X-750 alloy sheet
Panel 1A	Panel 1 after a 1 hour aluminization at 950 °C
Panel 1H	Panel 1A after 200 hour annealing at 1100 °C
Panel 2	Panel fabricated by EDM of X-750 alloy plate
Panel 2A	Panel 2 after a 3 hour aluminization at 850 °C
Panel 2H	Panel 2A after 200 hour annealing at 1100 °C

Panel 1 was aluminized for 1 hour at 950 °C and as-aluminized microstructure of the panel was consistent with the as-aluminized microstructure of the X-750 sheet (discussed and shown in section 3.1.1), which includes an outer layer of Al_3Ni_2 and β-NiAl with a β-NiAl innermost layer. A SEM image of the as-aluminized panel is shown in Figure 6.3. The pack cementation process produced a coating of uniform thickness on the outside of the panel as well as the channels on the inside of the panel.

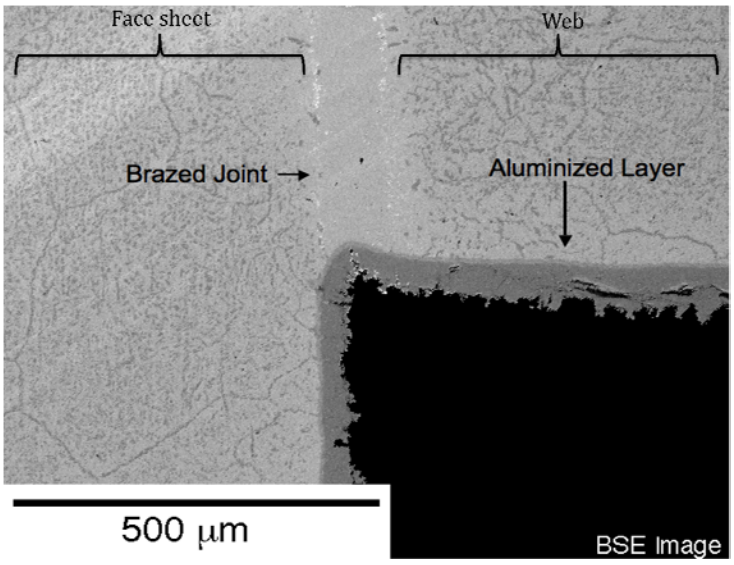

Figure 6.3: BSE image of Panel 1A – Rectangular channeled panel fabricated by brazing X-750 alloy sheet and aluminizing the panel for 1 hour at 950 °C.

Due to the elimination of the annealing step during the brazing cycle, the brazed joint is still clearly visible in Fig. 6.3. Although the microstructure differences are apparent at this step in the process, once the homogenization heat treatment is performed the brazed joint will be indistinguishable from the rest of the panel.

6.3 Annealing and Homogenization

Once panel 1 was aluminized it underwent a 200 hour homogenization heat treatment at 1100 °C in an Ar + 3% H_2 atmosphere. This treatment allowed for the aluminum to diffuse through the thickness of all the panel components, including joints. The EMPA concentration profiles across the joint are shown in Figure 6.4. The elemental concentrations are constant over the joint thickness, indicating the homogenization in the thickest component of panel 1H.

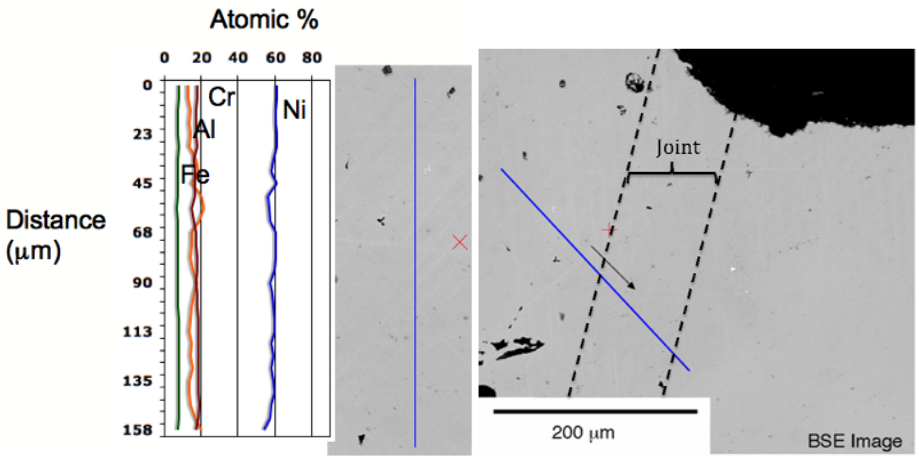

Figure 6.4: BSE image and EMPA concentration profiles of a joint in panel 1H – aluminized for 1 hour at 950 °C and annealed for 200 hours at 1100 °C.

6.4 High-Temperature Panel Testing

In order to test the thermostructural panels at high temperatures, panel 2 and panel 2H were actively cooled with water while being aggressively heated on one side of the panel with an oxy-acetylene torch. A thermocouple welded to the surface was used to measure the temperature of the torch heated surface of the panels during testing. Panels with the optimized geometry were tested in both panel 2 and panel 2H conditions in the setup shown in Figure 2.2, repeated here (Figure 6.5).

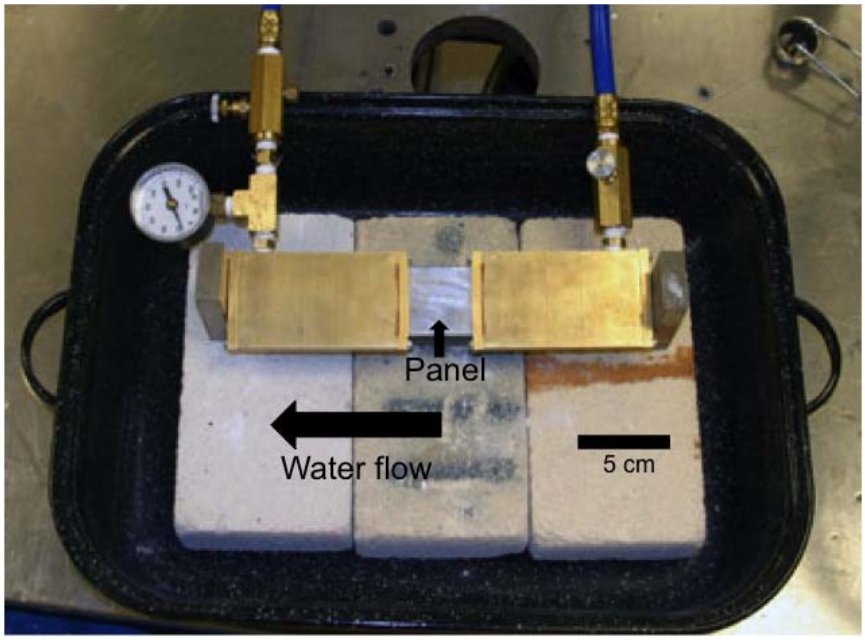

Figure 6.5: Image of the high-temperature testing apparatus for the actively-cooled thermostructural panels.

In order to directly compare the performance of panel 2 and panel, the mechanical loads they experienced were held constant. The water used as the cooling liquid was kept at a pressure of 0.4 MPa and a flow rate of 0.95 L/min (15.8 cm^3/s). Finite element analysis from the panel geometry code predicts the maximum combined stress occurs at a location along the top surface of the panel, with the specific location dependent on the channel dimensions. Output from the finite element analysis of a panel optimized for the as-received X-750 alloy is shown in Figure 6.6 (a). For panel 2, the failure mode predicted by the panel optimization code (for surface conditions below the maximum use temperature, T^*) was a tensile failure in the center of a cooling channel, see schematic in Figure 6.6(b). This is identical to the failure mode predicted for the panel 2 geometry under the conditions originally predicted in the panel geometry optimization code for fuel cooling conditions (90.5 cm^3/s at 0.9 MPa).

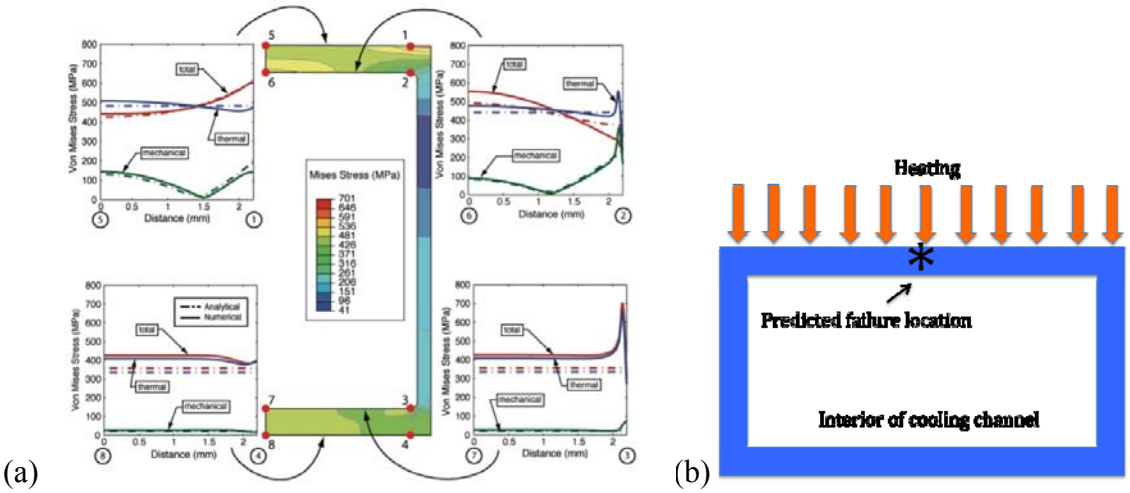

(a) (b)

Figure 6.6: (a) Finite element analysis output from panel geometry code showing the maximum combined stress at a position on the top surface of the panel (b) Schematic of the predicted failure location on a channel of the thermostructural panel optimized for the altered X-750 alloy.

Both panel 2 and panel 2H were heated with the torch on one side until failure. Although the failure did not occur directly at the thermocouple, both panels failed at similar distances from the thermocouple. The temperature measurement just before failure for panel 2 was 377 °C while panel 2H failed at a temperature measurement of 855 °C. Images of the panel surfaces after testing are shown in Figure 6.7 where it is clear that panel 2 had a larger perforation than panel 2H. Along with the improvement in mechanical and thermal resistance, images of the surface after testing reveal that the panel 2H also showed an increase in oxidation resistance. As seen in Figure 6.8, panel 2 has apparent discoloration on the surface near the failure while panel 2H does not show comparable degradation.

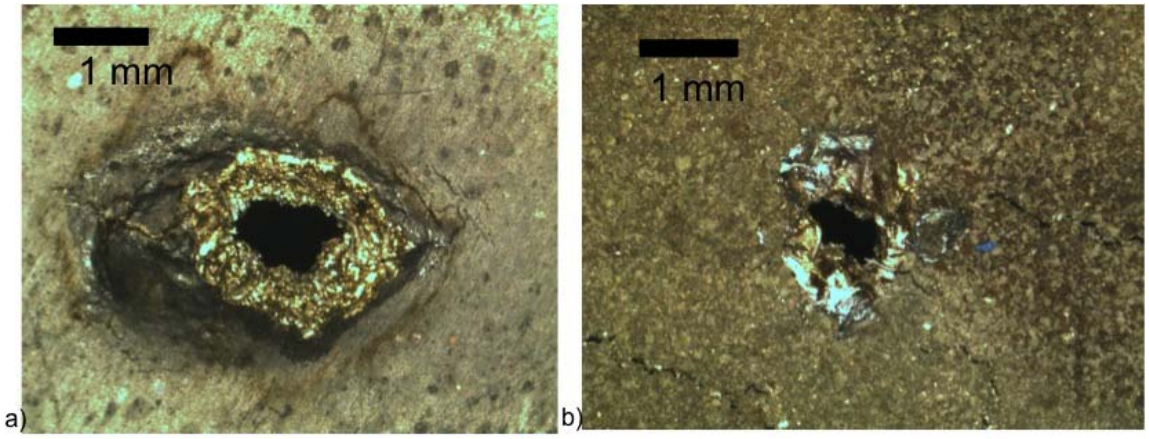

Figure 6.7: Optical images of the surface of the failed thermostructural panels. a) Panel 2 - X-750 alloy b) Panel 2H – altered X-750 alloy with 3 hour aluminization at 850 °C and 200 hour anneal at 1100 °C.

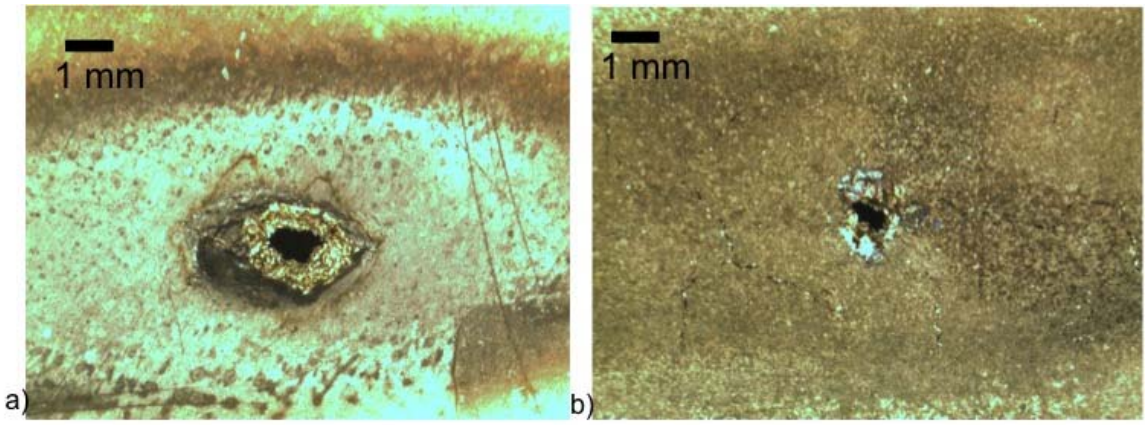

Figure 6.8: Optical images of the surface degradation near the failure points of the thermostructural panels. a) Panel 2 - X-750 alloy b) Panel 2H – altered X-750 alloy with 3 hour aluminization at 850 °C and 200 hour anneal at 1100 °C.

Upon further examination of the failure and the microstructure near the failure, panel 2H appears to have failed because the panel surface experienced temperatures above the maximum use temperature, T^* as evidenced by the reduced volume fraction of γ′ near the failure. Panel 2 seems to have failed due to exceeding the yield strength of the alloy. Etched images of various sections of panel 2H are shown in Figure 6.9 with a schematic of reference panel locations. The microstructure near the failure in panel 2H showed very limited and very coarse γ′ (Figure 6.9a) indicating that the excessive temperature on the surface resulted in the γ′ phase resolutioning into the matrix, reducing the strength of the alloy. The volume fraction of γ′ appears to have remained unchanged just below the thermocouple at about 40 volume % (Figure 6.9b), however there was significant coarsening near the surface. The microstructure in the center of the panel face sheet (Figure 6.9c) showed only slightly coarsened γ′ compared to the microstructure from a cool section of the panel (Figure 6.9d).

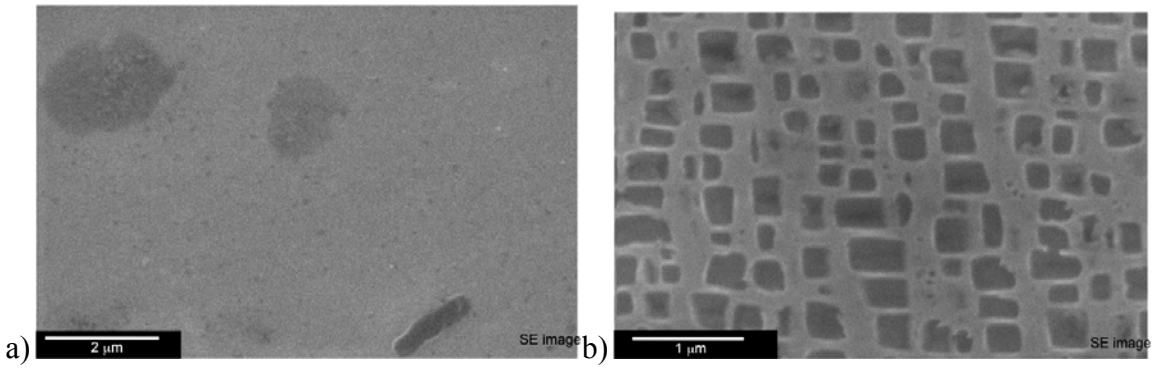

c) d)

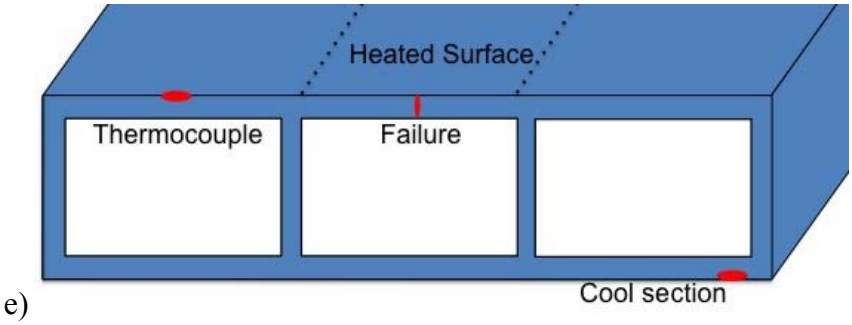

e)

Figure 6.9: SEM images of deeply etched positions in panel 2H after failure a) near the failure b) directly under the thermocouple c) from the center of the top face sheet under the thermocouple and d) from a cool region and a schematic e) of relative panel locations.

Comparing the calculated equilibrium volume fraction of γ′ in panel 2H as a function of temperature from Pandat^{TM} (Figure 5.1) with the images of the microstructure taken near

the failure, it is estimated that the local temperature at which the strengthened panel failed is about 1100 °C. Also the significantly reduced coarsening in the center of the face sheet below the thermocouple (Figure 6.9c) compared to directly below the thermocouple (Figure 6.9b) indicates that there was a temperature gradient across the thickness of the face sheet.

If the actual temperature at failure for panel 2H was near 1100 °C and the thermocouple measured 855 °C, it follows that the thermocouple measured a temperature approximately 245 °C lower than what the panel experienced at failure. With the similarity of the failure location relative to the thermocouple for panels 2 and 2H, it is possible to infer that the actual temperature panel 2 experienced at failure was approximately 245 degrees higher than the measured temperature of 377 °C resulting in a temperature at failure of 622 °C. With the finite element analysis in panel code, it is possible to calculate the stresses experienced by panel 2 with a surface temperature is 622 °C. In this case the maximum value of the combined thermal and mechanical stresses was predicted to be 620 MPa.

6.5 Discussion

6.5.1 Joining Process

It was possible to fabricate a rectangular channeled sandwich panel using the X-750 alloy with the braze tape (panel 1). The fixture held the pieces in the appropriate geometry

during the braze cycle to appropriate tolerances. As mentioned above, typically the braze cycle includes an annealing heat treatment in order to assure a homogenous joint. Due to the long heat treatment for the homogenization of aluminum after fabrication, it was possible to eliminate that step from the brazing procedure. The annealed panel did not show any deleterious effects from eliminating the annealing step during the brazing cycle. As shown in Figure 6.4, the homogenized panel (panel 2H) showed essentially no gradient in elemental concentrations across the joint ensuring similar material properties as in the remainder of the panel.

6.5.2 Machining Process

The EDM process allowed for the fabrication of a very thin walled structure, however this method was both time consuming and expensive. The small scale of this research made the EDM process feasible, yet for larger panels this process might be too expensive. Also, the EDM process changes the surface microstructure and leaves residual stresses in the material [65]. For larger scales it may be more beneficial to pursue a joining approach, such as demonstrated with the brazing fabrication.

6.5.3 Panel Homogenization

The microstructural evolution during the annealing of the panels 1 and 2 were identical to the annealing of the X-750 alloy reported in section 3.2.1 and was previously discussed in

section 3.5.2. The addition of joints in the panel increased the time necessary for homogenization of aluminum.

Both the brazed and EDM panels showed some geometrical inconsistencies after the annealing treatment. For the brazed panel, the average change of channel width from panel 1 to panel 1H was approximately 1.8% while the average change of channel height was approximately 4.5%. This panel was rapidly brought to the annealing temperature of 1100 °C. Initially the interior of the webbing and face sheets was still the pure X-750 alloy and at this temperature the X-750 alloy has extremely limited creep resistance [45] accounting for the change in panel geometry. The EDM panel also showed changes in the channel dimensions from panel 2 to panel 2H. The average change for channel height and width was approximately 2.2% and 1.2% respectively. In this case the panels were brought to the annealing temperature in a gradual manner, however the residual stresses from the EDM process were relaxed during annealing.

6.5.4 Panel Performance

Under the testing conditions, the cooling channels maintained a constant water pressure, keeping the mechanical loading similar for both the panels for a given temperature. Although the stresses due to thermal loading were different for the panels, panel 2 had a smaller thermal gradient and therefore would have experienced a reduced level of stress. Figure 6.10 is a schematic of yield strength versus temperature for both the strengthened and as-received X-750 alloys.

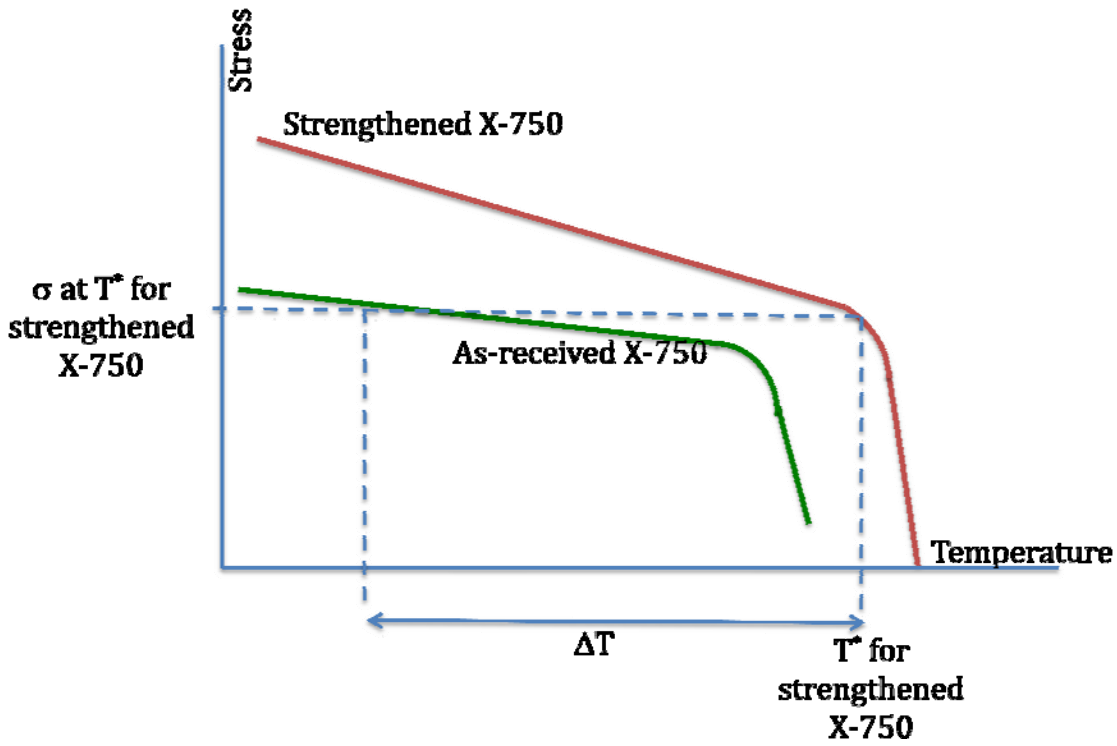

Figure 6.10: Schematic of yield strength as a function of temperature for the vapor phase strengthened and as-received X-750 alloy.

Knowing that panel 2H failed due to experiencing temperatures that exceeded T^*, the yield stress of the vapor phase strengthened alloy at T^* can be used as an approximation of the stress experienced by panel 2. From the chart in Figure 6.9, it is clear that that stress at T^* would exceed the yield stress of the as-received alloy at a much lower temperature, ΔT. With panel 2 failing at a temperature greater than 450 °C lower than panel 2H, it follows that the conditions described above are responsible for the failure of the panels.

The yield strength of the X-750 alloy at room temperature was 260 MPa, yet the ultimate tensile strength was 745 MPa. As mentioned in Section 6.4, the finite element analysis calculated combined thermal and mechanical stresses would have been 620 MPa. Although this is lower than the ultimate tensile strength, it is well above the yield strength of the material. With these stresses, the material deformed plastically altering the geometry of the channel, changing the stress concentrations and exceeding the ultimate tensile strength of the materal.

The improved oxidation resistance of panel 2H was due to the higher aluminum content and residual β layer on the surface of the panel. Although the deleterious effects of the residual β layer were discussed for room temperature applications in the previous chapter, in a high temperature oxidation environment the β layer provides more protection than hindrance.

6.5.5 Panel Mass Related to Processing Parameters

Combining the integration of models discussed in Chapter 4 and the experimental results of Chapter 5 it is possible to determine a relationship between the processing parameters and final minimum panel weight. For example, for a given aluminization time, a maximum yield strength can be determined. With the strength of the material, it is possible to calculate the minimum mass for a thermostructural panel-lined scramjet combustor (with dimension 0.148 x 0.5 x 2 m) for a constant heat transfer coefficient and equivalence ratio (related to cooling liquid flow rate) for the internal surfaces of a

scramjet combustor. The chart in Figure 6.11 displays this relationship for an aluminization temperature of 850 °C, a heat transfer coefficient of 445 W/m^{2}K and an equivalence ratio of 1.21 and a base alloy of X-750.

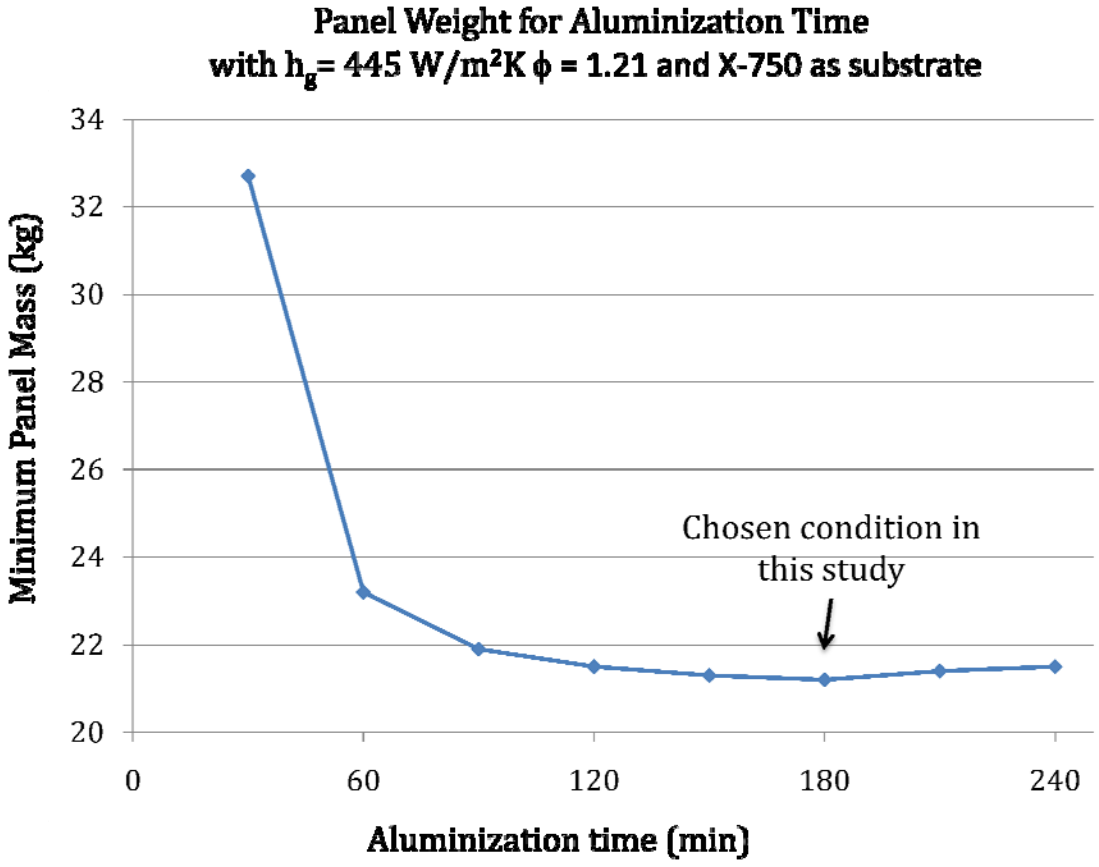

Figure 6.11: Relationship between minimum panel mass for a given aluminization time at 850 °C for a heat transfer coefficient of 445 W/m^{2}K and an equivalence ratio of 1.21 using X-750 as the substrate.

6.6 Summary

The feasibility of the vapor phase strengthening approach was determined in Chapter 3. Although the strengthening approach was validated, the application of the approach to a fabricated thermostructural panel was further demonstrated. The actively cooled panels were tested at high temperature in panel 2 and panel 2H conditions. Concerning the vapor phase strengthening and high temperature performance of thermostructural panels:

- Rectangular channeled thermostructural panels were successfully fabricated using two distinct methods – brazing and machining. The brazed panel (panel 1) was fabricated from pieces of flat sheet while the electric discharge machined panel (panel 2) was fabricated from a solid plate.

- The aluminized panels 1A and 2A yielded very similar microstructures to sheet samples discussed in Chapter 3. The coating structure was consistent over all the surfaces of the panel including the interior walls of the channels setting up the component for the homogenization treatment.

- After homogenization, the panel 1H had no deviation from the sheet samples in microstructure at the joints. This shows the joining process had no deleterious effects on the strengthened panel. The electric discharge machined panel (panel 2H) also showed no deviation in microstructure from the sheet samples.

- Both fabrication methods investigated proved to be feasible, although there was a slightly larger geometrical change for panel 1H than the flat sheet samples discussed in Chapter 3 for the brazed sample. When properly annealed, as in the case of the EDM panel (panel 2H), the average changes were very similar to the 2% changes in the feasibility samples.

- The high temperature performance of the vapor phase strengthened panel (panel 2H) showed improvements in mechanical properties, thermal resistance and oxidation resistance compared to panel 2. These were demonstrated with the difference in failure modes and the ability of panel 2H to withstand temperatures 478 °C higher than panel 2.

Chapter 7

Conclusions and Recommendations

7.1 Conclusions

This study has demonstrated the feasibility and performance of a vapor phase strengthened, refractory-lean, non-precipitation hardened alloy in a post-fabricated state. This was achieved by altering X-750 alloy by depositing aluminum on the surface and annealing to homogenize the material increasing the average aluminum concentration of the bulk all after the alloy was fabricated into a rectangular channeled sandwich panel. The following is a summary of the key components for the process:

- Aluminization via pack cementation successfully created an Al-rich layer near the surface of a variety of refractory-lean, non-precipitation hardened alloys without any significant change in dimensions.

- Annealing of the aluminized specimens homogenously distributed the aluminum through the 200 μm thick IN-625 sample and up to a depth of 250 μm in the

remaining samples, transforming initially highly formable materials into stronger, $\gamma + \gamma'$ precipitation hardened alloys.

- Panels with rectangular channels were fabricated by brazing wrought X-750 alloy sheet in a fixture to ensure proper geometry as well as by electric discharge machining from solid plate.

- Annealing of the aluminized specimens homogenously distributed the aluminum through the X-750 panel walls (up to 0.635 mm thick) transforming the initially formable material into a stronger, $\gamma + \gamma'$ precipitation hardened alloy. Thus it has been demonstrated that a solid solution Ni-based alloy can be fabricated into a panel and subsequently processed to achieve a precipitation strengthened Ni alloy in a previously unattainable geometry.

- An optimum microstructure was determined by integrating a trio of models including thermodynamic, yield strength and panel geometry. The optimum microstructure corresponded to an optimum aluminum content, which lead to an optimum aluminization process. In order to achieve the determined microstructure, heat treatment temperatures and aging times were established.

- Mechanical tests were performed to show the post-processing improvement in the mechanical properties. Even with a brittle residual β layer on the surface of tensile samples, yield strength was improved up to 340%.

- High temperature testing of thermostructural panels in the as-fabricated and post-fabrication processed conditions clearly showed the improvement of temperature capability, mechanical properties and oxidation resistance. The processed panel was able to withstand temperatures 478 °C higher than the as-fabricated panel.

- The integration of models along with experimental results permitted a relationship between processing parameters and final material properties to be developed. For example, a minimum thermostructural panel mass can be calculated for a given aluminization time.

- Although this study was exclusively directed towards a rectangular channeled, thin walled thermostructural panel, there is no reason why this strengthening process could not be used for other applications where a thin-walled, high-temperature capable structure is required. The applications may be varied, however, the results of this study would be limited to the refractory-lean nickel-base systems as the phases encountered along the diffusion path can drastically alter the feasibility of this process.

7.2 Recommendations for Future Research

- This study demonstrated the feasibility of the vapor phase strengthening approach for a small-scale thermostructural panel. Scaling up a component typically involves a new set of processing and fabrication challenges.

- The vapor phase strengthening process discussed in this study can be applied to additional metallic alloy systems. It will be necessary to determine the thermodynamic phases present for the alloy systems as well as the ability for aluminum to diffuse through any phases confirmed for the process.

- Different geometries for a thermostructual panel can use the vapor phase strengthening approach discussed in this study. For example, some scramjet designs include a cylindrical combustor. An actively cooled thermostructural panel could be employed for this application and will most likely require a thin walled geometry making the vapor phase strengthening approach feasible.

- Further studies on the temperature dependence of vapor phase strengthened material properties should be investigated and transmission electron microscopy studies be conducted to discern mechanisms of deformation. Also more detailed analysis of panel deformation following active cooling tests should be conducted.

Appendix

Full results of yield strength modeling for volume fractions 30 -70 % varying two precipitate population sizes (ds = 100-200 nm for the larger and dt = 20-35 nm for the smaller) as well as the relative volume fraction for the two populations (ft/fs). Reported values are for room temperature (RT) and in units of ksi.

Total volume fraction γ′ = 30

ft/fs	ds	dt	RT ys	ft/fs	ds	Dt	RT ys	ft/fs	Ds	dt	RT ys
0.1	100	20	**126**	0.2	100	20	**136**	0.3	100	20	142
	120	20	122		120	20	132		120	20	**367**
	140	20	119		140	20	129		140	20	351
	160	20	116		160	20	127		160	20	134
	180	20	114		180	20	125		180	20	132
	200	20	112		200	20	123		200	20	131
	100	25	126		100	25	134		100	25	141
	120	25	122		120	25	131		120	25	365
	140	25	119		140	25	128		140	25	349
	160	25	116		160	25	126		160	25	132
	180	25	114		180	25	124		180	25	130
	200	25	112		200	25	122		200	25	129
	100	30	125		100	30	133		100	30	139
	120	30	121		120	30	129		120	30	363
	140	30	118		140	30	127		140	30	347
	160	30	116		160	30	124		160	30	130
	180	30	114		180	30	122		180	30	128
	200	30	112		200	30	120		200	30	127
	100	35	124		100	35	132		100	35	141
	120	35	120		120	35	128		120	35	366
	140	35	117		140	35	125		140	35	350
	160	35	115		160	35	123		160	35	133
	180	35	113		180	35	121		180	35	131
	200	35	111		200	35	119		200	35	129
ft/fs	ds	dt	RT ys	ft/fs	ds	dt	RT ys	ft/fs	Ds	dt	RT ys
0.4	100	20	148	0.5	100	20	152	0.6	100	20	190
	120	20	308		120	20	239		120	20	245
	140	20	292		140	20	226		140	20	235

	160	20	272		160	20	232		160	20	226
	180	20	252		180	20	217		180	20	228
	200	20	137		200	20	220		200	20	218
	100	25	149		100	25	180		100	25	214
	120	25	310		120	25	268		120	25	269
	140	25	294		140	25	255		140	25	260
	160	25	274		160	25	260		160	25	250
	180	25	253		180	25	245		180	25	252
	200	25	138		200	25	248		200	25	243
	100	30	157		100	30	186		100	30	226
	120	30	317		120	30	274		120	30	281
	140	30	301		140	30	261		140	30	272
	160	30	281		160	30	266		160	30	262
	180	30	261		180	30	251		180	30	264
	200	30	145		200	30	255		200	30	255
	100	35	164		100	35	201		100	35	237
	120	35	**324**		120	35	**289**		120	35	**292**
	140	35	308		140	35	276		140	35	283
	160	35	288		160	35	281		160	35	273
	180	35	267		180	35	266		180	35	275
	200	35	152		200	35	270		200	35	265

Total volume fraction γ′ = 35

ft/fs	ds	dt	RT ys	ft/fs	ds	dt	RT ys	ft/fs	Ds	dt	RT ys
0.1	100	20	**128**	0.2	100	20	**139**	0.3	100	20	146
	120	20	124		120	20	135		120	20	142
	140	20	121		140	20	132		140	20	139
	160	20	118		160	20	129		160	20	137
	180	20	116		180	20	127		180	20	135
	200	20	114		200	20	125		200	20	133
	100	25	128		100	25	137		100	25	144
	120	25	124		120	25	133		120	25	140
	140	25	121		140	25	130		140	25	137
	160	25	118		160	25	128		160	25	135
	180	25	116		180	25	126		180	25	133
	200	25	114		200	25	124		200	25	131
	100	30	127		100	30	136		100	30	146
	120	30	123		120	30	132		120	30	142
	140	30	120		140	30	129		140	30	139
	160	30	117		160	30	126		160	30	137
	180	30	115		180	30	124		180	30	135
	200	30	113		200	30	122		200	30	133
	100	35	126		100	35	134		100	35	**148**
	120	35	122		120	35	130		120	35	144

	140	35	119		140	35	127		140	35	141
	160	35	116		160	35	125		160	35	139
	180	35	114		180	35	123		180	35	137
	200	35	112		200	35	121		200	35	135
ft/fs	ds	dt	RT ys	ft/fs	ds	dt	RT ys	ft/fs	Ds	dt	RT ys
0.4	100	20	151	0.5	100	20	179	0.6	100	20	224
	120	20	376		120	20	307		120	20	306
	140	20	360		140	20	318		140	20	294
	160	20	143		160	20	299		160	20	281
	180	20	141		180	20	279		180	20	284
	200	20	140		200	20	285		200	20	271
	100	25	162		100	25	204		100	25	244
	120	25	386		120	25	332		120	25	326
	140	25	371		140	25	343		140	25	314
	160	25	154		160	25	324		160	25	301
	180	25	152		180	25	304		180	25	304
	200	25	150		200	25	310		200	25	291
	100	30	177		100	30	222		100	30	260
	120	30	401		120	30	350		120	30	341
	140	30	385		140	30	361		140	30	329
	160	30	168		160	30	342		160	30	316
	180	30	167		180	30	322		180	30	320
	200	30	165		200	30	328		200	30	306
	100	35	131		100	35	231		100	35	272
	120	35	**405**		120	35	360		120	35	**354**
	140	35	389		140	35	**371**		140	35	342
	160	35	173		160	35	352		160	35	329
	180	35	171		180	35	332		180	35	332
	200	35	169		200	35	337		200	35	319

Total volume fraction γ′ = 40

ft/fs	ds	dt	RT ys	ft/fs	ds	dt	RT ys	ft/fs	Ds	dt	RT ys
0.1	100	20	**130**	0.2	100	20	**141**	0.3	100	20	148
	120	20	126		120	20	137		120	20	145
	140	20	122		140	20	134		140	20	142
	160	20	120		160	20	131		160	20	139
	180	20	117		180	20	129		180	20	137
	200	20	115		200	20	127		200	20	135
	100	25	129		100	25	139		100	25	146
	120	25	125		120	25	135		120	25	142
	140	25	122		140	25	132		140	25	139
	160	25	119		160	25	129		160	25	137
	180	25	117		180	25	127		180	25	134
	200	25	115		200	25	125		200	25	133

	100	30	128		100	30	137		100	30	155
	120	30	124		120	30	133		120	30	151
	140	30	121		140	30	130		140	30	148
	160	30	118		160	30	127		160	30	146
	180	30	116		180	30	125		180	30	143
	200	30	114		200	30	123		200	30	142
	100	35	127		100	35	136		100	35	**156**
	120	35	123		120	35	132		120	35	152
	140	35	120		140	35	129		140	35	149
	160	35	117		160	35	126		160	35	147
	180	35	115		180	35	124		180	35	144
	200	35	113		200	35	122		200	35	143
ft/fs	ds	dt	RT ys	ft/fs	ds	dt	RT ys	ft/fs	Ds	dt	RT ys
0.4	100	20	154	0.5	100	20	210	0.6	100	20	257
	120	20	151		120	20	391		120	20	374
	140	20	148		140	20	373		140	20	359
	160	20	145		160	20	385		160	20	343
	180	20	143		180	20	200		180	20	348
	200	20	142		200	20	198		200	20	331
	100	25	182		100	25	239		100	25	277
	120	25	179		120	25	420		120	25	394
	140	25	176		140	25	402		140	25	379
	160	25	174		160	25	414		160	25	363
	180	25	172		180	25	229		180	25	368
	200	25	170		200	25	227		200	25	351
	100	30	197		100	30	253		100	30	295
	120	30	194		120	30	434		120	30	411
	140	30	191		140	30	415		140	30	397
	160	30	188		160	30	427		160	30	381
	180	30	186		180	30	243		180	30	386
	200	30	185		200	30	241		200	30	368
	100	35	**203**		100	35	265		100	35	310
	120	35	200		120	35	**446**		120	35	**427**
	140	35	197		140	35	428		140	35	412
	160	35	195		160	35	440		160	35	396
	180	35	193		180	35	255		180	35	402
	200	35	191		200	35	253		200	35	384

Total volume fraction γ' = 45

ft/fs	ds	dt	RT ys	ft/fs	ds	dt	RT ys	ft/fs	Ds	dt	RT ys
0.1	100	20	**131**	0.2	100	20	**142**	0.3	100	20	150
	120	20	126		120	20	138		120	20	146
	140	20	123		140	20	135		140	20	143
	160	20	120		160	20	132		160	20	140

	180	20	118		180	20	129		180	20	138
	200	20	116		200	20	127		200	20	136
	100	25	130		100	25	140		100	25	153
	120	25	126		120	25	136		120	25	149
	140	25	122		140	25	133		140	25	145
	160	25	119		160	25	130		160	25	143
	180	25	117		180	25	128		180	25	141
	200	25	115		200	25	126		200	25	139
	100	30	129		100	30	138		100	30	160
	120	30	125		120	30	134		120	30	156
	140	30	121		140	30	131		140	30	152
	160	30	118		160	30	128		160	30	150
	180	30	116		180	30	126		180	30	148
	200	30	114		200	30	124		200	30	146
	100	35	128		100	35	139		100	35	**166**
	120	35	124		120	35	135		120	35	163
	140	35	120		140	35	132		140	35	159
	160	35	117		160	35	129		160	35	157
	180	35	115		180	35	126		180	35	154
	200	35	113		200	35	124		200	35	153
ft/fs	ds	dt	RT ys	ft/fs	ds	dt	RT ys	ft/fs	Ds	dt	RT ys
0.4	100	20	173	0.5	100	20	248	0.6	100	20	294
	120	20	169		120	20	492		120	20	454
	140	20	166		140	20	241		140	20	438
	160	20	164		160	20	239		160	20	418
	180	20	162		180	20	237		180	20	398
	200	20	160		200	20	235		200	20	283
	100	25	204		100	25	270		100	25	317
	120	25	200		120	25	514		120	25	477
	140	25	197		140	25	264		140	25	461
	160	25	195		160	25	261		160	25	442
	180	25	192		180	25	259		180	25	421
	200	25	191		200	25	258		200	25	306
	100	30	212		100	30	286		100	30	338
	120	30	208		120	30	530		120	30	498
	140	30	205		140	30	280		140	30	482
	160	30	203		160	30	278		160	30	462
	180	30	201		180	30	276		180	30	442
	200	30	199		200	30	274		200	30	326
	100	35	**219**		100	35	296		100	35	356
	120	35	216		120	35	**541**		120	35	**516**
	140	35	213		140	35	290		140	35	500
	160	35	210		160	35	288		160	35	481
	180	35	208		180	35	186		180	35	460

	200	35	206		200	35	284		200	35	345

Total volume fraction γ′ = 50

ft/fs	ds	dt	RT ys	ft/fs	ds	dt	RT ys	ft/fs	ds	dt	RT ys
0.1	100	20	**131**	0.2	100	20	**143**	0.3	100	20	151
	120	20	127		120	20	138		120	20	147
	140	20	123		140	20	135		140	20	144
	160	20	120		160	20	132		160	20	141
	180	20	118		180	20	130		180	20	138
	200	20	115		200	20	128		200	20	136
	100	25	130		100	25	141		100	25	163
	120	25	126		120	25	136		120	25	158
	140	25	122		140	25	133		140	25	155
	160	25	119		160	25	130		160	25	152
	180	25	117		180	25	128		180	25	150
	200	25	114		200	25	125		200	25	148
	100	30	129		100	30	139		100	30	170
	120	30	125		120	30	134		120	30	166
	140	30	121		140	30	131		140	30	163
	160	30	118		160	30	128		160	30	160
	180	30	115		180	30	126		180	30	158
	200	30	113		200	30	124		200	30	156
	100	35	128		100	35	140		100	35	**173**
	120	35	123		120	35	136		120	35	169
	140	35	120		140	35	132		140	35	165
	160	35	117		160	35	129		160	35	163
	180	35	114		180	35	127		180	35	160
	200	35	112		200	35	125		200	35	158
ft/fs	ds	dt	RT ys	ft/fs	ds	dt	RT ys	ft/fs	ds	dt	RT ys
0.4	100	20	198	0.5	100	20	283	0.6	100	20	166
	120	20	194		120	20	280		120	20	347
	140	20	191		140	20	277		140	20	329
	160	20	189		160	20	274		160	20	341
	180	20	186		180	20	272		180	20	156
	200	20	185		200	20	270		200	20	144
	100	25	232		100	25	305		100	25	367
	120	25	228		120	25	301		120	25	548
	140	25	225		140	25	298		140	25	530
	160	25	222		160	25	296		160	25	542
	180	25	220		180	25	294		180	25	357
	200	25	218		200	25	292		200	25	356
	100	30	243		100	30	324		100	30	391
	120	30	239		120	30	320		120	30	**572**
	140	30	236		140	30	317		140	30	554

	160	30	234		160	30	315		160	30	566
	180	30	231		180	30	313		180	30	381
	200	30	230		200	30	311		200	30	380
	100	35	**253**		100	35	**341**		100	35	155
	120	35	250		120	35	337		120	35	336
	140	35	246		140	35	334		140	35	317
	160	35	244		160	35	332		160	35	329
	180	35	242		180	35	330		180	35	145
	200	35	240		200	35	328		200	35	143

Total volume fraction γ′ = 55

ft/fs	ds	dt	RT ys	ft/fs	ds	dt	RT ys	ft/fs	ds	dt	RT ys
0.1	100	20	**131**	0.2	100	20	**143**	0.3	100	20	151
	120	20	126		120	20	138		120	20	147
	140	20	123		140	20	135		140	20	144
	160	20	120		160	20	132		160	20	141
	180	20	117		180	20	129		180	20	138
	200	20	115		200	20	127		200	20	136
	100	25	130		100	25	140		100	25	168
	120	25	125		120	25	136		120	25	163
	140	25	121		140	25	132		140	25	160
	160	25	118		160	25	129		160	25	157
	180	25	116		180	25	127		180	25	155
	200	25	114		200	25	125		200	25	153
	100	30	128		100	30	140		100	30	**177**
	120	30	124		120	30	136		120	30	173
	140	30	120		140	30	132		140	30	169
	160	30	117		160	30	129		160	30	167
	180	30	115		180	30	127		180	30	164
	200	30	112		200	30	124		200	30	162
	100	35	127		100	35	142		100	35	180
	120	35	123		120	35	138		120	35	176
	140	35	119		140	35	134		140	35	172
	160	35	116		160	35	132		160	35	170
	180	35	113		180	35	129		180	35	167
	200	35	111		200	35	127		200	35	165
ft/fs	ds	dt	RT ys	ft/fs	ds	dt	RT ys	ft/fs	ds	dt	RT ys
0.4	100	20	227	0.5	100	20	**163**	0.6	100	20	167
	120	20	223		120	20	159		120	20	**405**
	140	20	220		140	20	156		140	20	161
	160	20	217		160	20	154		160	20	159
	180	20	215		180	20	152		180	20	157
	200	20	213		200	20	150		200	20	155
	100	25	255		100	25	159		100	25	163

	120	25	251		120	25	155		120	25	400
	140	25	248		140	25	152		140	25	157
	160	25	245		160	25	150		160	25	154
	180	25	243		180	25	148		180	25	152
	200	25	241		200	25	146		200	25	151
	100	30	268		100	30	156		100	30	159
	120	30	264		120	30	152		120	30	396
	140	30	261		140	30	149		140	30	153
	160	30	258		160	30	146		160	30	150
	180	30	256		180	30	144		180	30	148
	200	30	254		200	30	142		200	30	147
	100	35	**280**		100	35	153		100	35	155
	120	35	276		120	35	149		120	35	393
	140	35	273		140	35	146		140	35	149
	160	35	270		160	35	143		160	35	147
	180	35	268		180	35	141		180	35	145
	200	35	266		200	35	139		200	35	143

Total volume fraction γ′ = 60

ft/fs	ds	dt	RT ys	ft/fs	ds	dt	RT ys	ft/fs	ds	dt	RT ys
0.1	100	20	**130**	0.2	100	20	**142**	0.3	100	20	151
	120	20	125		120	20	137		120	20	146
	140	20	121		140	20	134		140	20	143
	160	20	118		160	20	131		160	20	140
	180	20	116		180	20	128		180	20	138
	200	20	113		200	20	126		200	20	135
	100	25	128		100	25	140		100	25	181
	120	25	124		120	25	135		120	25	177
	140	25	120		140	25	131		140	25	174
	160	25	117		160	25	128		160	25	171
	180	25	114		180	25	126		180	25	168
	200	25	112		200	25	124		200	25	166
	100	30	127		100	30	140		100	30	185
	120	30	123		120	30	136		120	30	181
	140	30	119		140	30	132		140	30	177
	160	30	116		160	30	129		160	30	175
	180	30	113		180	30	126		180	30	172
	200	30	111		200	30	124		200	30	170
	100	35	126		100	35	143		100	35	**201**
	120	35	121		120	35	139		120	35	196
	140	35	118		140	35	135		140	35	193
	160	35	115		160	35	132		160	35	190
	180	35	112		180	35	129		180	35	188
	200	35	110		200	35	127		200	35	185

ft/fs	ds	dt	RT ys	ft/fs	ds	dt	RT ys	ft/fs	ds	dt	RT ys
0.4	100	20	158	0.5	100	20	**163**	0.6	100	20	**168**
	120	20	154		120	20	159		120	20	164
	140	20	150		140	20	156		140	20	161
	160	20	147		160	20	154		160	20	159
	180	20	145		180	20	152		180	20	157
	200	20	143		200	20	150		200	20	155
	100	25	285		100	25	159		100	25	163
	120	25	281		120	25	155		120	25	159
	140	25	277		140	25	152		140	25	156
	160	25	275		160	25	150		160	25	154
	180	25	272		180	25	147		180	25	152
	200	25	270		200	25	145		200	25	150
	100	30	**300**		100	30	156		100	30	159
	120	30	296		120	30	152		120	30	155
	140	30	293		140	30	149		140	30	152
	160	30	290		160	30	146		160	30	150
	180	30	287		180	30	144		180	30	148
	200	30	285		200	30	142		200	30	146
	100	35	148		100	35	152		100	35	155
	120	35	144		120	35	149		120	35	152
	140	35	141		140	35	145		140	35	149
	160	35	138		160	35	143		160	35	147
	180	35	136		180	35	141		180	35	145
	200	35	134		200	35	138		200	35	143

Total volume fraction $\gamma' = 65$

ft/fs	ds	dt	RT ys	ft/fs	ds	dt	RT ys	ft/fs	ds	dt	RT ys
0.1	100	20	**128**	0.2	100	20	140	0.3	100	20	163
	120	20	123		120	20	136		120	20	159
	140	20	120		140	20	132		140	20	155
	160	20	116		160	20	129		160	20	152
	180	20	114		180	20	126		180	20	150
	200	20	111		200	20	124		200	20	148
	100	25	127		100	25	138		100	25	191
	120	25	122		120	25	134		120	25	187
	140	25	118		140	25	130		140	25	183
	160	25	115		160	25	127		160	25	180
	180	25	112		180	25	124		180	25	178
	200	25	110		200	25	122		200	25	175
	100	30	125		100	30	141		100	30	196
	120	30	121		120	30	137		120	30	191
	140	30	117		140	30	133		140	30	188
	160	30	114		160	30	130		160	30	185

	180	30	111		180	30	127		180	30	182
	200	30	109		200	30	125		200	30	180
	100	35	124		100	35	**144**		100	35	**200**
	120	35	120		120	35	139		120	35	196
	140	35	116		140	35	135		140	35	192
	160	35	113		160	35	132		160	35	189
	180	35	110		180	35	130		180	35	186
	200	35	108		200	35	127		200	35	184
ft/fs	ds	dt	RT ys	ft/fs	ds	dt	RT ys	ft/fs	ds	dt	RT ys
0.4	100	20	**157**	0.5	100	20	**163**	0.6	100	20	**167**
	120	20	153		120	20	159		120	20	163
	140	20	149		140	20	155		140	20	160
	160	20	146		160	20	153		160	20	158
	180	20	144		180	20	150		180	20	156
	200	20	142		200	20	149		200	20	154
	100	25	153		100	25	158		100	25	162
	120	25	149		120	25	154		120	25	158
	140	25	146		140	25	151		140	25	155
	160	25	143		160	25	149		160	25	153
	180	25	140		180	25	146		180	25	151
	200	25	138		200	25	144		200	25	149
	100	30	150		100	30	144		100	30	158
	120	30	146		120	30	155		120	30	154
	140	30	142		140	30	151		140	30	151
	160	30	140		160	30	148		160	30	149
	180	30	137		180	30	145		180	30	147
	200	30	135		200	30	143		200	30	145
	100	35	147		100	35	152		100	35	155
	120	35	143		120	35	148		120	35	151
	140	35	140		140	35	145		140	35	148
	160	35	137		160	35	142		160	35	146
	180	35	135		180	35	140		180	35	144
	200	35	132		200	35	138		200	35	142

Total volume fraction γ′ = 70

ft/fs	ds	dt	RT ys	ft/fs	ds	dt	RT ys	ft/fs	ds	dt	RT ys
0.1	100	20	**125**	0.2	100	20	138	0.3	100	20	**148**
	120	20	121		120	20	134		120	20	143
	140	20	117		140	20	130		140	20	140
	160	20	114		160	20	127		160	20	137
	180	20	111		180	20	124		180	20	134
	200	20	109		200	20	122		200	20	132
	100	25	124		100	25	136		100	25	145
	120	25	119		120	25	131		120	25	140

	140	25	116		140	25	128		140	25	137
	160	25	112		160	25	125		160	25	134
	180	25	110		180	25	122		180	25	131
	200	25	107		200	25	120		200	25	129
	100	30	123		100	30	141		100	30	142
	120	30	118		120	30	137		120	30	138
	140	30	114		140	30	133		140	30	134
	160	30	111		160	30	130		160	30	131
	180	30	109		180	30	127		180	30	128
	200	30	106		200	30	125		200	30	126
	100	35	122		100	35	**141**		100	35	140
	120	35	117		120	35	136		120	35	135
	140	35	113		140	35	133		140	35	132
	160	35	110		160	35	130		160	35	129
	180	35	107		180	35	127		180	35	126
	200	35	105		200	35	125		200	35	124
ft/fs	ds	dt	RT ys	ft/fs	ds	dt	RT ys	ft/fs	ds	dt	RT ys
0.4	100	20	**155**	0.5	100	20	**161**	0.6	100	20	**165**
	120	20	151		120	20	157		120	20	161
	140	20	147		140	20	154		140	20	158
	160	20	144		160	20	151		160	20	156
	180	20	142		180	20	149		180	20	154
	200	20	140		200	20	147		200	20	152
	100	25	152		100	25	157		100	25	160
	120	25	147		120	25	153		120	25	157
	140	25	144		140	25	149		140	25	154
	160	25	141		160	25	147		160	25	151
	180	25	138		180	25	144		180	25	149
	200	25	136		200	25	142		200	25	147
	100	30	149		100	30	153		100	30	157
	120	30	144		120	30	149		120	30	153
	140	30	141		140	30	146		140	30	150
	160	30	138		160	30	143		160	30	147
	180	30	135		180	30	141		180	30	145
	200	30	133		200	30	139		200	30	143
	100	35	146		100	35	150		100	35	153
	120	35	142		120	35	146		120	35	149
	140	35	138		140	35	143		140	35	146
	160	35	135		160	35	140		160	35	144
	180	35	133		180	35	138		180	35	142
	200	35	131		200	35	136		200	35	140

Summary of largest yield strength for a given total volume fraction and population ratio:

Total Volume Fraction									
ft/fs	**30**	**35**	**40**	**45**	**50**	**55**	**60**	**65**	**70**
0.1	126	128	130	131	131	131	130	128	125
0.2	136	139	141	142	143	143	142	144	141
0.3	367	148	156	166	173	177	201	200	148
0.4	324	405	203	219	253	280	300	157	155
0.5	289	371	446	541	341	163	163	163	161
0.6	292	354	427	516	572	405	168	167	165

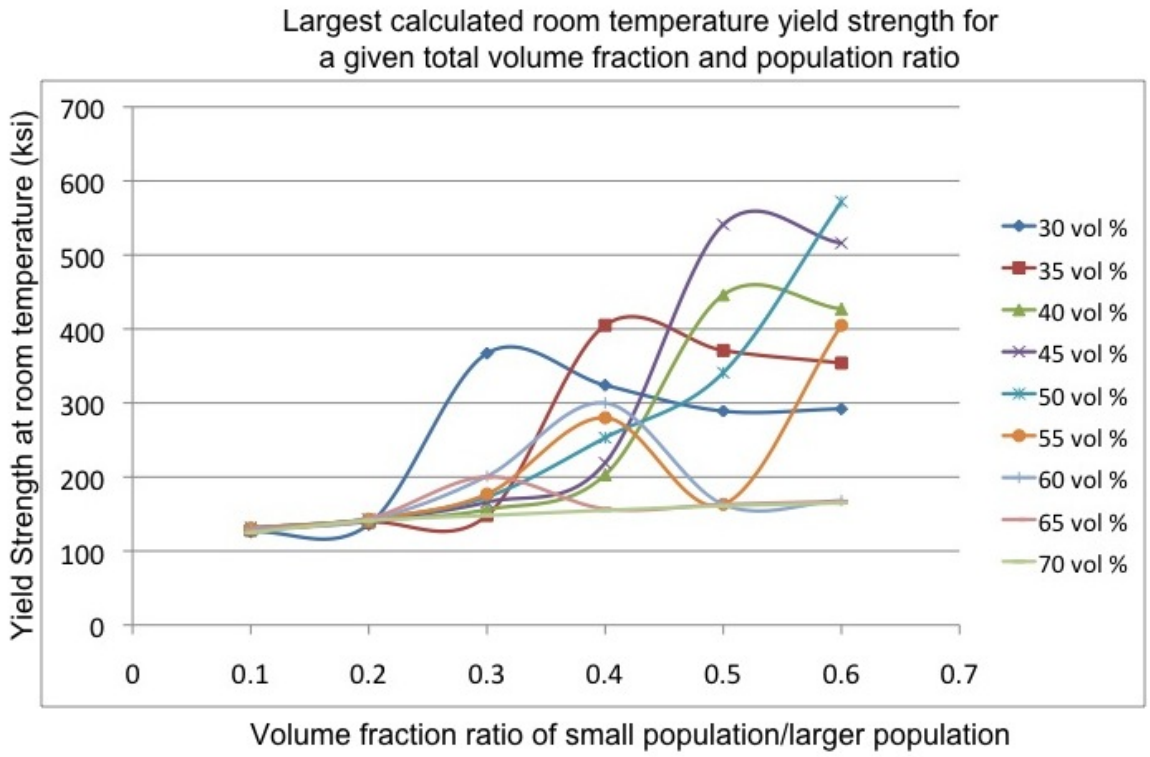

References

[1] N. Wicks, J.W. Hutchinson, Int. J. Solids Struct. 38 (2001) 5165.

[2] A.G. Evans, J.W. Hutchinson, N.A. Fleck, M.F. Ashby, H.N.G. Wadley, Progr. Mater. Sci. 46 (2001) 309.

[3] L. Valdevit, J.W. Hutchinson, A.G. Evans, Int. J. Solids Struct. 41 (2004) 5104.

[4] M.V. Nathal, J.D. Whittenberger, M.G. Hebsur, P.T. Kantzos, D.L. Krause, Superalloys 2004 (eds. K.A. Green, T.M. Pollock, H. Harada, T.E. Howson, R.C. Reed, J.J. Schirra, S. Walston) TMS, (2004) 431.

[5] F.W. Zok, H.J. Rathbun, Z. Wei, A.G. Evans, Int. J. Solids Struct. 40 (2003) 5707.

[6] J.F. Rakow and A.M. Waas, Journal of Spacecraft and Rockets, 42 (2005) 832.

[7] J.F. Rakow and A.M. Waas, AIAA Journal 45 (2007) 329.

[8] S. Hyun, A.M. Karlsson, S. Torquato, A.G. Evans, Int. J. Solids Struct. 40 (2003) 6989.

[9] M. Durand-Charre, The Microstructure of Superalloys, Gordon and Breach, Singapore, 1997.

[10] R. Reed, The Superalloys Fundamentals and Applications, Cambridge University Press, United Kingdom, 2006.

[11] R. Streiff and J.M. N'Gandu Muamba, Thin Solid Films 119 (1984) 291.

[12] D.C. Tu and L.L. Seigle, Thin Solid Films 95 (1982) 47.

[13] M.E. Glicksman, Diffusion in Solids: Field Theory, Solid-State Principles, and Applications, John Wiley & Sons, New York, 2000.

[14] W.D. Callister, Jr., Materials Science and Engineering an Introduction, John Wiley & Sons, Inc., USA, 2003.

[15] C.J. Kuehmann and P.W. Voorhees, Ostwald Ripening in Ternary Alloys, Met. Mater. Trans. A 27A (1996) 937.

[16] A.J. Ardell, The Effect of Volume Fraction on Particle Coarsening: Theoretical Considerations, Acta Metallurgica, 20 (1972) 61.

[17] R.W. Kozar, A. Suzuki, W.W. Milligan, J.J. Schirra, M.F. Savage, T.M. Pollock Metallurgical and Materials Transactions, 40A (2009) 1588.

[18] J.R. Nicholls and D.J. Stephenson, "High-Temperture Coatings for Gas Turbines," *Intermetallic Compounds: Vol. 2*, eds. J.H. Westbrook and R.L. Fleischer, (John Wiley & Sons), 1995.

[19] J.R. Nicholls, Designing Oxidation-Resistant Coatings, J. Materials 52 (2000) 28.

[20] R. Mévrel, C. Duret, and R. Pichoir, Pack Cementation Processes, Materials Science and Technology, 2 (1986), 201.

[21] D.C. Dunand, A.M. Hodge and C. Schuh, Materials Science and Technology, 18 (2002) 326.

[22] A.M. Hodge and D.C. Dunand, Intermetallics 9 (2001) 581.

[23] S.J. Johnson, B. Tryon and T.M. Pollock, Acta Materialia 56 (2008) 4577.

[24] B.K. Gupta, L.L. Seigle, Thin Solid Films, 73 (1980) 365.

[25] R. Sivakumar and L.L. Seigle, Metallurgical Transactions A, 7A (1976) 1073.

[26] G.W. Goward and D.H. Boone, Oxidation of Metals, Vol. 3, No. 5 (1971) 475.

[27] D.K. Das, V. Singh, S.V. Joshi, Met. Mater. Trans. A 29A (1998) 2173.

[28] A.K. Sarkhel and L.L Seigle, Metallurgical Transactions A, 9A (1978) 1467.

[29] M.M.P. Janssen, G.D. Rieck, Trans. TMS-AIME, 1967, vol. 239, 1372.

[30] A.J. Hickl and R.W. Heckel, Metallurgical Transactions A, 6A (1975) 431.

[31] L. Valdevit, Z. Wei, C. Mercer, F.W. Zok, A.G. Evans, International Journal of Solids and Structures, 43 (2006) 4888.

[32] N. Vermaak, L. Valdevit and A.G. Evans, Materials Property Profiles for Actively Cooled Panels: An Illustration for Scramjet Applications, Metallurgical and Materials Transactions A, 40A (2009) 877.

[33] S. Gu, T.J. Lu, A.G. Evans, International Journal of Heat and Mass Transfer, 44 (2001) 2163.

[34] D.S. Duvall, W.A. Owczarski and D.F. Paulonis, Welding Journal, 53 (1974) 203.

[35] R.L. Peaslee, Practical Welding Today, Vol. 8, No. 6, 2004.

[36] R.L. Peaslee, The Fabricator, November 1998.

[37] A. Rabinkin, International Brazing & Soldering Conference Proceedings, (2000).

[38] M. Nakahashi, S. Suenaga, M. Shirokane, H. Takeda, Materials Transactions, Vol. 33, No. 1 (1992) 60.

[39] W.D MacDonald, T.W. Eagar, Annual Review Materials Science, 46 (1992) 22.

[40] W.D. Zhuang, T.W. Eagar, Welding Research Supplement, Dec. 1997, 526-s.

[41] C.C. Tennenhouse, Welding Journal, Oct. 1997.

[42] INCONEL® alloy 625 specifications, Special Metals Corporation, Sept. 2004.

[43] INCONEL® alloy 693 specifications, Special Metals Corporation, Feb. 2005.

[44] Haynes 214 alloy specifications, Haynes International Inc, 1996.

[45] Haynes X750 alloy specifications, Haynes International Inc, 2004.

[46] ASTM Standard E8/EM8, 2009, "Standard Testing Methods for Tension Testing of Metallic Materials," ASTM International, West Conshohocken, PA, 2009, DOI: 10.1520/E0008_E0008M-09, www.astm.org.

[47] AMDRY DF-6A braze specifications, Sulzer Metco, 2000.

[48] P.E.A. Turchi, L. Kaufman, Zi-Kui Liu, Calphad 30 (2006) 70.

[49] M.K. Miller and M.G. Burke, Applied Surface Science, 67 (1993) 292.

[50] G.C. Wood and F.H. Stott, High Temperature Corrosion, (ed. R.A. Rapp) National Association of Corrosion Engineers, (1983) 227.

[51] W.H. Tian, C.S. Han, M. Nemoto, Intermetallics 7 (1999) 59.

[52] H.L. Huang, Y.Z. Chen, D. Gan, Mater. Sci. Eng. A 206 (1996) 215.

[53] S.V. Divinski, S.T. Frank, U. Söderwall, E.H.R. Herzig, Acta Materialia, 12 (1998) 4369.

[54] N. Voudouris, C. Christoglou, G.N. Angelopoulos, Surf. Coat. Tech 141 (2001) 275.

[55] M. Watanabe, Z. Horita, T. Sano, M. Nemoto, Acta Metall. Mater. 42 (1994) 10.

[56] M. Meyers and K Chawla, Mechanical Behavior of Materials 2nd Edition, Cambridge University Press, United Kingdom, 2009.

[57] S. Bose, High Temperature Coatings, Elsevier Science & Technology Books, 2007.

[58] N. Dupin, I. Ansara, H.L. Lukas, and B. Sundman, An Assessment of the Al-Ni System, Journal of Alloys and Compounds, 247 (1997) 20.

[59] N. Dupin, I. Ansara, and B. Sundman, Thermodynamic re-assessment of the ternary system Al-Cr-Ni, Calphad 25 (2001) 279.

[60] J.C. Zhao, V. Ravikumar, and A.M. Beltran, Phase Precipitation and phase stability in nimonic 263, Metall. Mat. Trans. A, 32A (2001) 2735.

[61] U. Trabandt, B. Esser, D. Koch, R. Knoche, and G. Tumino, Ceramic Matrix Composites Life Cycle Testing Under Reusable Launcher Environmental Conditions, International Journal of Applied Ceramic Technology, 2 (2005) 150.

[62] D.J. Chellman and A.J. Ardell, The Coarsening of γ′ Precipitates at Large Volume Fractions, Acta Metallurgica, 22 (1974) 577.

[63] ASM Metals Handbook, Vol19 Fracture and Fatigue, ASM International, 1996.

[64] G. Camus, L. Guillaumat, S. Baste, Development of Damage in a 2D Woven C/SiC Composite Under Mechanical Loading: I. Mechanical Characterization, Composites Science and Technology 56 (1996) 1363.

[65] M. Barash, Electric Spark Machining, Int. J. Mach. Tool Des. Res. 2 (1962) 331.